ARCHIVES OF MECHANICS
Arch. Mech. **76** (1-2), 93–141, 2024, DOI: 10.24423/aom.4459

A size-dependent functionally graded nanocomposite Mindlin plate model based on consistent generalized continuum theory

M. Z. ROSHANBAKHSH, S. M. TAVAKKOLI*)

Department of Civil Engineering, Shahrood University of Technology, Shahrood, Iran, e-mail): mtavakkoli@shahroodut.ac.ir*

This paper presents an effective consistent-continuum model to analyse the behaviour of functionally graded nanocomposite (FG-NC) Mindlin plates based on the consistent couple stress theory (CCST) and the non-classical finite element method. A novel unified form is presented based on the Halpin–Tsai model to capture the small-scale heterogeneity, which can simultaneously consider the grading effects of the matrix and reinforcement phases along with the dispersion distribution through the plate thickness. To meet the C^1 continuity requirements of the couple stress theory, a four-node rectangular element is adopted by using the Hermitian approach and in the way of a sub-parametric manner. The element has 20 degrees of freedom (DOF) at each node, which is reduced to 12 DOF in a bending mode without stretching deformation. FG-NC plates' bending, free vibration, and buckling behaviour are investigated. Graphene oxide (GO), reduced graphene oxide (rGO), and silver-reduced graphene oxide (Ag-rGO) are considered for the dispersed phase. Size-dependent optimal values for the material and geometrical properties of the FG-NC plate model are presented, which minimize its mass with the frequency constraint. The effects of various parameters such as grading index, weight fraction, dispersion pattern, filler aspect/thickness ratio, and length scale parameter are examined, and benchmark examples are provided.

Key words: C-CST, size-dependent finite element, FG-nanocomposite Mindlin plate, graphene-based reinforcements.

1. Introduction

Nanocomposite (NC) plates are widely used nowadays due to their high flexibility without reducing strength, light density, high surface-area-to-volume ratio, high fracture resistance and energy adsorption, thermal/electrical/biological features, scratch resistance as well as excellent vibrational and fatigue behaviour [1–4]. A nanocomposite plate generally refers to structural elements made of nanocomposite materials, representing composites in which the reinforcement phase has dimensions of about nanometres. On the other hand, the dimensions of the size-dependent nanocomposite plate are close to the characteristic length, for example, the plate thickness can be around micrometres.

The multi-scale character plays a key role in the size-dependent behaviour of such structural elements, while the classical (Cauchy) continuum mechanics theory (C-CMT) is unable to model this feature. In this respect, a set of methods known as generalized continuum mechanics theories (G-CMT) have incorporated size effects into the underlying formulation of C-CMT by using various approaches, which are generally divided into two categories: non-local and local [5]. The former considers a weighted integral for the relevant parameters, e.g. the stress is considered as a weighted spatial average of the strain or a micro-scale variable. In this way, the length scale parameter is incorporated into the underlying formulation through the weight function. A limited non-locality refers to a situation in which higher gradients of the desired parameter are defined at each point. Such an approach is called gradient or higher-grade [6]. On the other hand, the generalized local continuum also called the higher-order continuum, is enriched by microstructure at each geometrical point. Microstructure requires small-scale degrees of freedom Micromorphic and Micropolar theories fall into this category and are described by nine and six additional small-scale degrees of freedom at each point, respectively [7]. Despite the many advantages of these theories, their multi-scale modelling is incompatible with the point-by-point continuity concept of CMT. In this regard, a mono-scale version of the Micropolar theory the so-called couple stress theory (CST) or the Mindlin–Tiersten–Koiter couple stress theory (MTK-CST) has been developed, which ignores the independence assumption of small-scale DOF and relates it to the macro-scale translational DOF [8, 9]. However, Eringen [7] revealed that MTK-CST suffers from the indeterminacy of the spherical part of the couple-stress tensor, which is due to the trace-free character of the bend-twist tensor. A widely used modified version of MTK-CST called MCST was presented by Yang *et al.* [10]. Emerging the symmetric part of the couple stress tensor instead of its asymmetric form can be considered the main character of MCST.

There are many works devoted to the analysis of homogeneous/inhomogeneous structural elements based on MCST in the literature [11, 12]. Hadjesfandiari and Dargush [13] disclosed some notable drawbacks of M-CST. They showed that the indeterminacy of MTK-CST still exists in MCST. On the other hand, to reduce the number of material modulus, an additional moment equilibrium equation is considered, which violates Newton's third law. In this regard, Hadjesfandiari and Dargush [13–15] revealed the antisymmetric character of the couple-stress tensor and showed that the double-layer shear force-stresses can model the couple-stress effect. As a result, all inconsistencies in CST and M-CST such as the complexity of underlying formulations, indeterminacy of the spherical part of the couple-stress tensor, and ambiguity in boundary conditions will be resolved. Hereupon, the last updated version of CST is named the consistent cou-

ple stress theory (C-CST). C-CST has been used and developed in various fields since its emergence. Hadjesfandiari and co-workers [16–19] developed C-CST based piezoelectricity and thermo-elasticity. VAGHEFPOUR and ARVIN [20] performed a nonlinear free vibration analysis of cantilever pre-actuated piezoelectric nano-beams by using C-CST. DENG and DARGUSH [21] presented a novel mixed variational approach to enrich the consistent couple stress theory, which removes the continuity requirements of the C-CST. ABBASPOUR and ARVIN [22] investigated free and forced vibration as well as a thermal buckling analysis of multilayered piezoelectric micro-plates under consistent couple stress assumptions PATEL *et al.* [23] presented a C-CST-based constitutive model for a micro-beam under large elastic deflection. The semi-analytical singularity removal method is used to extract the slope along the deformed neutral axis. A comparative study with experimental results is presented, which shows a good agreement. HADJESFANDIARI and DARGUSH [24] examined various versions of the couple stress theory in a comparative study. They showed that the pure torsion behavior of micro-diameter copper wires modelled under C-CST, unlike other versions, completely agrees with experimental models. SOROUSH *et al.* [25] studied the stability analysis of nanotweezers and nanoswitches based on the consistent couple stress theory. They developed a bilayer model using the Gurtin–Murdoch surface elasticity and C-CST assumptions.

The presented model shows a good agreement with its experimental counterpart. The results revealed that the surface layer can lead to an increase in the instability threshold. In recent years, nano-sized components have been widely used as reinforcements in phased composites. However, as the size decreases some issues such as aggregation, agglomeration, load transfer mechanism, and dissolution must be controlled [26–28]. Carbon nanotube (CNT), graphene (G), graphene platelet (GPL), graphene oxide (GO), reduced graphene oxide (rGO), and some modified versions such as silver-reduced graphene oxide (Ag-rGO) nano-hybrid are the most important nano-sized reinforcements. Investigations show that the one-dimensional character of CNT and the high surface energy of graphene (due to its strong intermolecular π-π interaction) cause a non-uniform dispersion in the matrix material, which leads to agglomeration [27]. The oxidized form of graphene, also called graphene oxide (GO), comprises oxygen-containing functional groups (hydroxyl, carbonyl, epoxy and carboxyl) which cause better dispersion, a larger interlayer gap of graphene oxide and more comfortable exfoliation [28, 29]. The reduction of oxygen-content functional groups of GO in various manners including chemical, thermal, and electrochemical revive some mechanical/chemical/electrical properties which is known as reduced graphene oxide (rGO) [28–30]; rGO under an incomplete reduction can suffer many overall defects [30]. In this context, some modifier agents such as metal nano-particles can be employed to decorate filler (on the surface) so that act as spacers for

maintaining the primitive structure of the filler as well as properties improver through their features [29]. Various modifying nano-particles can be employed such as Ferrum (Fe), Silver (Ag), Nickel (Ni), and so on. Guo *et al.* [29] investigated the design of highly thermally conductive Ag/rGO/polyimide nanocomposite. The results revealed that the thermal conductivity of nanocomposite records the highest value when the mass ratio of rGO to Ag is 4:1 and the mass fraction of Ag/rGO fillers is equal to 15 wt%. Yang *et al.* [31] examined the influence of modified rGO on various properties of the copper matrix composite by using silver and cerium agents. Micro-mechanics, macro-mechanics, manufacturing process, and optimal design are the most important areas of these fields. Several analytical, numerical and semi-empirical plans for modelling the heterogeneous structure of Macro/Micro/Nano phased composites are available in the literature, which estimate the effective thermo-mechanical properties and other desired fields [2, 32–34]. However, there are important issues that should be addressed including porosity, structural defects, size-dependent behaviour, uncertainty, and functionally graded manner of the shape, size, orientation, and mechanical properties of the dispersed phase. On the other hand, the analysis of macro-mechanical behaviour is critically affected by the micromechanical model. Hence, it seems essential to model the size-dependent and at the same time mono-scale behaviour.

Consistent mono-scale size-dependent modelling is achieved using C-CST. However, many complexities also arise in the underlying formulation. In this respect, one of the most important topics in the CST is the continuity concept and its numerical requirements under the finite element method In fact, CST assumes the micro-rotational DOFs are dependent on the macro-translational displacement field u, which leads to the existence of the second-order derivatives of u in the curvature relation as a deformation measurement tool. Therefore, to capture the weak form integrability requirements, displacement field u must pass the C^1 continuity. To this end, the continuity of the field variable u as well as its normal derivative $\partial u/\partial n$ along the element boundaries is required. In fact, the weak solution must be a function of the Sobolev space $H^2(\Omega)$, which in turn requires C^1 continuity for the ansatz since C^0 is not sufficient. The most common ways to remedy this are: providing C^1 continuous elements (conforming) using very smooth functions, nonconforming elements such that the solution is provided in $H^1(\Omega)$ or even only $L^2(\Omega)$ but not in $H^2(\Omega)$, and reformulation of the problem (typically in the form of a saddle point problem) as a mixed formulation so that higher order derivatives are avoided [35–37]. There are several studies concerning analysing composite structural elements using various versions of CST and committed to the C^1 continuity in the literature. Nguyen *et al.* [38] studied bending, free vibration, and buckling analysis of MCST-based FG microplates by using the seventh-

order quasi-3D shear deformation theory and isogeometric approach. FARZAM and HASSANI [39] performed an isogeometric analysis of in-plane functionally graded porous microplates. Static displacement, fundamental frequencies, and critical buckling load were extracted by employing the hyperbolic shear deformation theory and MCST assumptions. MA *et al.* [40] provide an analytical solution of the bending and free vibration of the simply supported microplate using the modified couple stress theory. The results revealed the importance of the small-scale effects, especially when the length-scale ratio approaches one. ZHANG *et al.* [41] presented a non-classical finite element model of microplate based on MCST. THAI *et al.* [42] investigated the free vibration and buckling behaviour of GPL-based composite plates with various dispersion patterns of filler. They showed natural frequencies and critical buckling load have a direct relation with weight fraction values and material length scale-to-thickness ratios while in the case of length-to-thickness ratios it is inverse. WU and HU [43] examined the bending and free vibration of a simply supported FG microplate as well as simply supported multi-layered graphene sheets surrounded in an elastic medium based on C-CST. APOSTOLAKIS and DARGUSH [37] presented the Ritz spline method for two and three-dimensional C-CST-based free vibration problems.

Interestingly some modes showed a direct relationship with the characteristic length ratio, while the rest were less affected or unaffected. WU and his co-workers [44–46] investigated free vibration of the simply supported FG-microplate/Piezoelectricmicroplate under various conditions and surrounded in an elastic medium based on C-CST. WU and HSU [47] derived displacement, stress, and frequencies of a simply-supported FG microplate. WU and LU [48] carried out a 3D analysis of the bending behaviour of a simply-supported FG piezoelectric microplate under closed-circuit surface conditions by using the small-scale Hermitian C^2 finite layer method. WU *et al.* [49] employed the penalty function method to present a C^0 8-node quadrilateral and 20-node hexahedral elements for the C-CST problem. MAO *et al.* [50] presented a non-conforming 4-node element with 3-DOF per node for the C-CSTbased analysis of the orthotropic Kirchhoff plate. FARZAM and HASSANI [51] performed an isogeometric analysis of the free vibration and buckling of the FG-rGO-epoxy nanocomposite plate using the refined plate theory (RPT) and M-CST. As discussed earlier, developing size-dependent models are essential for analysing nanocomposite structures due to their small-scale character. There are several works in the literature based on M-CST devoted to composite/nanocomposite plates [52]. However, C-CST provides a consistent underlying formulation that is suitable for mono-scale modelling of homogeneous/composite structures involving only one length scale parameter. From this point of view, modelling the bending, free vibration and buckling behaviour of C-CST-based composite plates committed

to C^1 continuity reinforced by nanofillers under the arbitrary load and boundary conditions is an interesting topic. On the other hand, the gradual change of constituent material in the phased composites/nanocomposites can lead to higher performance of the final product. Besides, modified versions of graphene reduce common issues in graphene-based nanocomposites, such as aggregation and agglomeration. A review of the literature reveals that in most of the works dedicated to functionally graded composite/nanocomposite plates, the graded parameter is the volume fraction of the reinforcement phase, and the reinforcement phase is made of graphene platelets [42]. However, gradual changes in the shape, size, orientation, and mechanical properties of the dispersed phase as well as the properties of the matrix material can also be considered. In this respect, a preferred design for conventional functionally graded reinforced nanocomposite involves the addition of gradual changes in the separate mechanical properties of the matrix and modified graphene-based reinforcements such as GO, rGO, Ag-rGO.

This paper presents a mono-scale size-dependent analysis of functionally graded nanocomposite (FG-NC) Mindlin plates based on the consistent couple stress theory (CCST) and the non-classical finite element method. The small-scale heterogeneities of FG-NC plates are homogenized in a novel unified form by using the Halpin–Tsai model. In this respect, the elasticity modulus of composite constituents as well as the distribution of dispersed phase can be continuously changed through the plate thickness. A four-node rectangular element is adopted by using the Hermitian approach and in the context of a sub-parametric model to capture the C^1 continuity requirements of the couple stress theory. The element has 20-DOF at each node, which is reduced to 12-DOF in a bending mode without stretching deformation. The proposed model is applied to investigate the bending, frequency analysis, and buckling behaviour of FG-NC plates. Concerning the geometrically nonlinear character of the buckling analysis, the von Karman nonlinearity is used to construct nonlinear kinematics. In this regard, in an explicit manner, it is shown that the von Karman nonlinear terms disappear in curvature, twist, and bending tensors. An improved family of graphene including graphene oxide (GO), reduced graphene oxide (rGO), and silver-reduced graphene oxide (Ag-rGO) nano-hybrid are considered to meet some critical issues such as agglomeration. The matrix phase is modelled by epoxy and copper. Optimal values for the material and geometrical properties of the FG-NC model are presented, which minimize its mass with the frequency constraint. A comprehensive study is conducted to disclose the effects of various parameters such as grading index, weight fraction, dispersion patterns, filler aspect/thickness ratio, length scale parameter, load type, and boundary conditions, in which some results are benchmark values.

2. Consistent-couple stress theory (C-CST)

The asymmetric force-stress tensor σ is the main distinguishing feature of the higher-order theories, which originates from the presence of couples per unit area [8]. From a kinematic point of view, the couple stress requires a small-scale rotational partner, as its energy conjugate. Based on CST, the small-scale rotational partner is related to the macro-translational DOF, which leads to a mono-scale character. Two tools for measuring deformation in CST are the symmetric macro-strain tensor E (in the sense of Green–Lagrange strain), as conjugate energy of the symmetric part of the force-stress tensor, and the micro-curvature tensor Γ [8]:

$$E = \tfrac{1}{2}(\nabla_0 u + (\nabla_0 u)^T + \nabla_0 u.(\nabla_0 u)^T), \tag{2.1}$$

$$\Gamma = -E \times \nabla_0, \tag{2.2}$$

where ∇_0 is the del operator with respect to the reference coordinates and u is the classical displacement vector. A small displacement gradient in comparison to unity (i.e., $|\nabla_0 u| \ll 1$) allows linearization in the following form:

$$E \approx \tfrac{1}{2}(\nabla u + (\nabla u)^T) = \varepsilon, \quad \nabla = \nabla_0, \tag{2.3}$$

$$\Gamma \approx -\varepsilon \times \nabla = \omega, \tag{2.4}$$

where ∇ is the del operator with respect to the current coordinates, ε and ω denote small symmetric macro-strain tensor and gradient of small micro-rotation vector φ, respectively. The small micro-rotation vector ϕ is related to the left curl of the displacement field u (i.e., $\nabla \times u/2$), and hereupon, the small micro-curvature ω is called the bend-twist tensor and has a trace-free character (i.e., $\omega_{ii} = \phi_{i,i} = 0$). The asymmetric tensor ω can be expressed as the sum of two parts, the symmetric tensor χ and the skew-symmetric tensor k. The former refers to a twist whereas the latter refers to a bending deformation [13]. MTK-CST uses the asymmetric form of the curvature tensor, while M-CST uses the symmetric one. However, in C-CST the couple stress tensor μ and its energy conjugate are antisymmetric. In this way, a couple stress effect can be described as double-layer shear force-stresses [15]. This leads to the elimination of common inconsistencies in the MTK-CST and M-CST [13–15]. Therefore, deformation measurement tools in linear C-CST include the symmetric macro-strain tensor and the antisymmetric mean curvature tensor (see Fig. 1). The mean curvature tensor can be expressed in the form of a true vector [13]:

$$k = \tfrac{1}{4}\nabla \times (\nabla \times u), \tag{2.5}$$

the component form of the mean curvature vector (2.5) in the orthogonal Cartesian coordinate system can be written as $\frac{1}{4}e_{iml}e_{jkl}\frac{\partial u_k}{\partial x_m \partial x_j}e_i$, where e_{ijk} and e_i

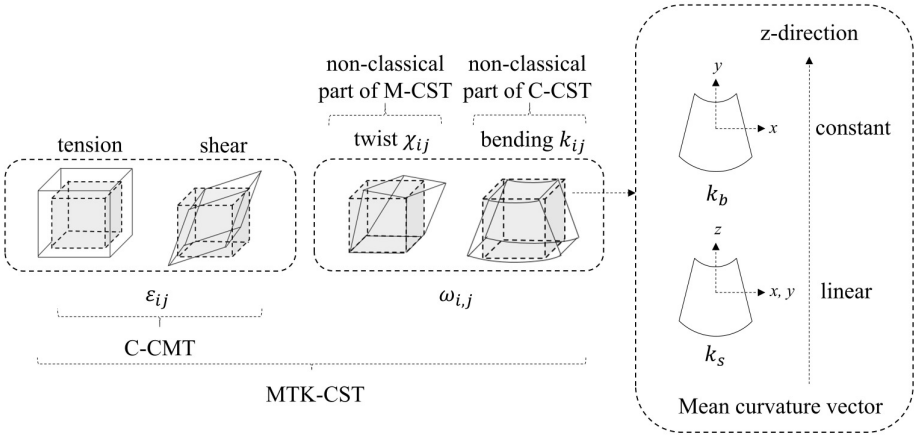

Fig. 1. Comparison of C-CMT and CST tools for deformation measuring, and interpretation of mean curvature components via infinitesimal element.

denote the permutation symbol and basis vectors, respectively The CCST-based elastic energy can be written in terms of the symmetric part of the force-stress tensor σ_s, the macro-strain tensor ε, the couple-stress vector μ and the mean curvature vector k:

$$U = \frac{1}{2}\int_V \sigma_s : \varepsilon \, dV - \int_V \mu.k \, dV. \tag{2.6}$$

The couple-stress vector μ is dual to the antisymmetric couple-stress tensor $\mu_{ij} = e_{ijk}\mu_k$. The constitutive relations for linear elastic isotropic centrosymmetric materials under the C-CST approach can be defined as follows [13]:

$$\begin{aligned} \sigma_s &= \bar{\lambda} tr(\varepsilon) I + 2\bar{\mu}\varepsilon, \\ \mu &= -8\eta k, \end{aligned} \tag{2.7}$$

where $tr(\cdot)$ and I denote the trace of the enclosed tensor and the identity matrix, respectively. $\bar{\lambda}$ and $\bar{\mu}$ are the Lame constants; $\eta = \bar{\mu}\iota^2$ is a couple stress elastic factor; ι is a length scale parameter that represents microstructure effects. The elastic energy comparable to M-CST can be obtained by scaling $\eta \to \eta/4$ or $\iota \to \iota/2$ [13, 14, 43].

3. CCSTbased FG-NC Mindlin plate model

Consider a rectangular FG-NC plate under arbitrary loads and boundary conditions made of isotropic elastic material in the Cartesian coordinate system (x, y, z) as shown in Fig. 2a. The plate's length, width, and thickness are

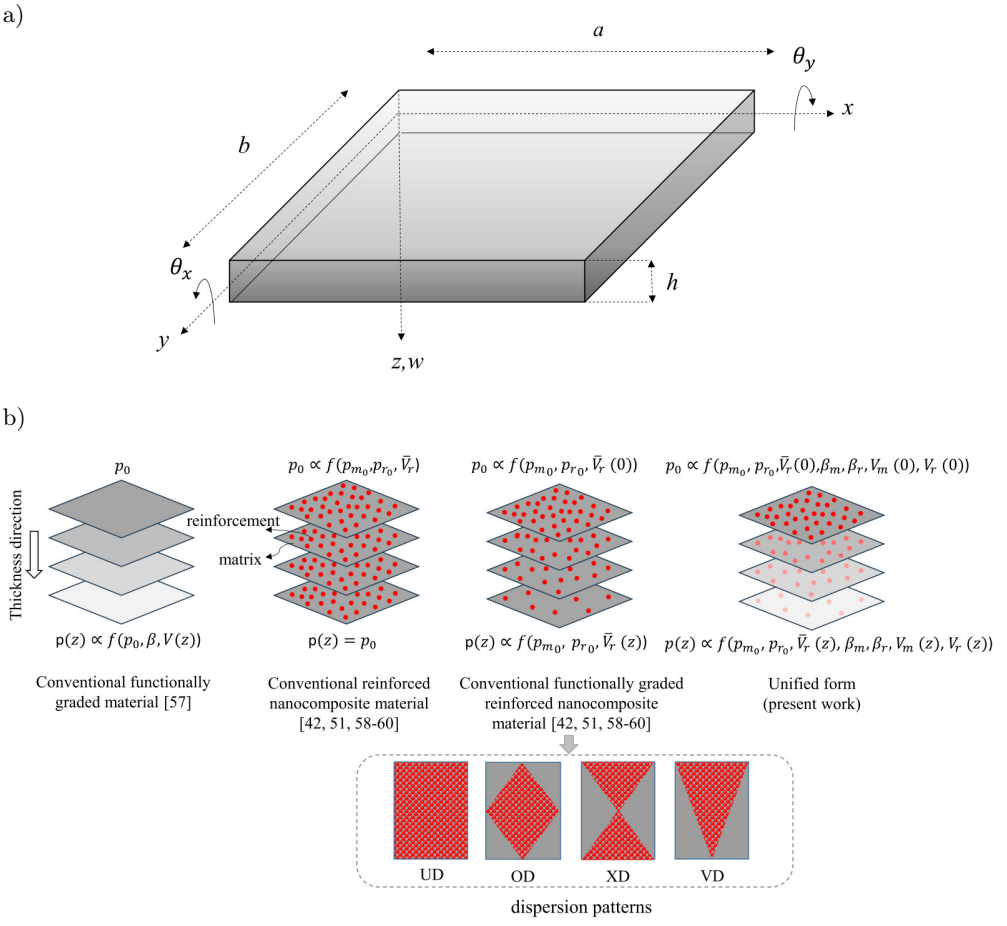

FIG. 2. a) Geometry and degrees of freedom of FG-NC plate; b) unified form of grading and dispersion patterns.

denoted by a, b and h, respectively. The displacement field $\boldsymbol{u}$ based on the Mindlin plate theory can be defined as [53]:

$$
\begin{aligned}
u_x(x,y,z,t) &= u(x,y,t) - z\theta_x(x,y,t),\\
u_y(x,y,z,t) &= v(x,y,t) - z\theta_y(x,y,t),\\
u_z(x,y,z,t) &= w(x,y,t),
\end{aligned}
\tag{3.1}
$$

u, v, and w are the middle plane displacements of the plate. θ_x and θ_y are the rotations of the transverse normal to the middle plane with respect to axes y and x, respectively. The present work obeys the linear discipline. However, to capture geometrical nonlinear sense for the buckling analysis, von Karman

nonlinearity assumptions are used. Hence, it is necessary to show the effect of these assumptions on the curvature tensor as well as the strain tensor.

3.1. CSTbased von Karman strain and curvature tensors and linearization

Concerning Eqs. (2.1) and (3.1), the small change in a plate element shape allows the omission of high-order terms (i.e., $(\partial u/\partial x)(\partial u/\partial x)$, $(\partial u/\partial x)(\partial u/\partial y), \ldots$). However, when the rotation of the transverse normal is moderate (i.e., 10°–15° in a macro-scale vision [53]), terms $(\partial w/\partial x)$, $(\partial w/\partial x)$, $(\partial w/\partial y)(\partial w/\partial y)$, and $(\partial w/\partial x)(\partial w/\partial y)$ are small enough to keep strain small, but yet large so that cannot be ignored. In this sense the von Karman strains related to the displacement field (3.1) can be constructed from Eq. (2.1):

$$\begin{aligned} &\varepsilon_x = \frac{\partial u}{\partial x} - z\frac{\partial \theta_x}{\partial x} + \varepsilon_x^{NL}, \quad \varepsilon_y = \frac{\partial v}{\partial y} - z\frac{\partial \theta_y}{\partial y} + \varepsilon_y^{NL}, \quad \varepsilon_z = 0, \\ &\gamma_{xy} = \frac{\partial u}{\partial y} + \frac{\partial v}{\partial x} - z\frac{\partial \theta_x}{\partial y} - z\frac{\partial \theta_y}{\partial x} + \gamma_{xy}^{NL}, \ \gamma_{xz} = \frac{\partial w}{\partial x} - \theta_x, \ \gamma_{yz} = \frac{\partial w}{\partial y} - \theta_y, \end{aligned} \tag{3.2}$$

superscript *NL* stands for nonlinear terms. The nonlinear strain terms can be expressed in the vector form as:

$$\varepsilon^{NL} = \left[\varepsilon_x^{NL} \ \varepsilon_y^{NL} \ \gamma_{xy}^{NL}\right]^T = \frac{1}{2}\left[\left(\frac{\partial w}{\partial x}\right)^2 \ \left(\frac{\partial w}{\partial y}\right)^2 \ 2\frac{\partial w}{\partial x}\frac{\partial w}{\partial y}\right]^T, \tag{3.3}$$

concerning Eq. (3.2), when the deflection to the plate thickness ratio is small (say $w/h \leq 0.2$ in a macro-scale vision), the nonlinear vector ε^{NL} can be neglected. In this respect, inplane strains ε_b and transverse shear strains ε_s are obtained corresponding to Eq. (2.3) as:

$$\varepsilon_b = \left[\varepsilon_x \ \varepsilon_y \ \gamma_{xy}\right]^T = \varepsilon_b^0 - z\varepsilon_b^1, \tag{3.4}$$

$$\varepsilon_s = \left[\gamma_{yz} \ \ \gamma_{xz}\right]^T = \left[\frac{\partial w}{\partial y} - \theta_y \ \ \frac{\partial w}{\partial x} - \theta_x\right]^T, \tag{3.5}$$

$$\varepsilon_b^0 = \left[\frac{\partial u}{\partial x} \ \ \frac{\partial v}{\partial y} \ \ \frac{\partial v}{\partial x} + \frac{\partial u}{\partial y}\right]^T, \quad \varepsilon_b^1 = \left[\frac{\partial \theta_x}{\partial x} \ \ \frac{\partial \theta_y}{\partial y} \ \ \frac{\partial \theta_y}{\partial x} + \frac{\partial \theta_x}{\partial y}\right]^T. \tag{3.6}$$

Next, the mean curvature vector k is determined. To this end, the curvature tensor $\hat{\Gamma}$ can be expanded using an arbitrary strain tensor $\hat{\varepsilon}$, which meets von Karman assumptions. In this regard, by using Eq. (2.2), and inducing the linearization concepts of Eq. (2.4), the component form of the curvature tensor is obtained in the orthogonal Cartesian coordinate system as follows:

$$\hat{\Gamma} = e_{jkr}\frac{\partial \hat{\varepsilon}_{ij}}{\partial x_k} e_i \otimes e_r, \tag{3.7}$$

or

$$\hat{\Gamma}_x = -\frac{\partial \hat{\varepsilon}_{xy}}{\partial z} + \frac{\partial \hat{\varepsilon}_{xz}}{\partial y}, \quad \hat{\Gamma}_y = -\frac{\partial \hat{\varepsilon}_{yz}}{\partial x} + \frac{\partial \hat{\varepsilon}_{yx}}{\partial z}, \quad \hat{\Gamma}_z = -\frac{\partial \hat{\varepsilon}_{zx}}{\partial y} + \frac{\partial \hat{\varepsilon}_{zy}}{\partial x},$$

$$\hat{\Gamma}_{xy} = \frac{\partial \hat{\varepsilon}_x}{\partial z} - \frac{\partial \hat{\varepsilon}_{xz}}{\partial x}, \quad \hat{\Gamma}_{yx} = -\frac{\partial \hat{\varepsilon}_y}{\partial z} + \frac{\partial \hat{\varepsilon}_{yz}}{\partial y}, \quad \hat{\Gamma}_{xz} = -\frac{\partial \hat{\varepsilon}_x}{\partial y} + \frac{\partial \hat{\varepsilon}_{xy}}{\partial x}, \tag{3.8}$$

$$\hat{\Gamma}_{zx} = -\frac{\partial \hat{\varepsilon}_{zy}}{\partial z} + \frac{\partial \hat{\varepsilon}_z}{\partial y}, \quad \hat{\Gamma}_{yz} = -\frac{\partial \hat{\varepsilon}_{yx}}{\partial y} + \frac{\partial \hat{\varepsilon}_y}{\partial x}, \quad \hat{\Gamma}_{zy} = \frac{\partial \hat{\varepsilon}_{zx}}{\partial z} - \frac{\partial \hat{\varepsilon}_z}{\partial x},$$

by using the von Karman strain (3.2) in Eq. (3.8), the micro-curvature tensor ω and its symmetric and antisymmetric parts, that is, the twist tensor χ and the mean curvature tensor k, are obtained as follows:

$$\omega_x = \frac{1}{2}\left(\frac{\partial \theta_y}{\partial x} + \frac{\partial^2 w}{\partial x \partial y}\right), \quad \omega_y = \frac{1}{2}\left(-\frac{\partial^2 w}{\partial y \partial x} - \frac{\partial \theta_x}{\partial y}\right),$$

$$\omega_z = \frac{1}{2}\left(\frac{\partial \theta_x}{\partial y} - \frac{\partial \theta_y}{\partial x}\right),$$

$$\omega_{xy} = \frac{1}{2}\left(-\frac{\partial \theta_x}{\partial x} - \frac{\partial^2 w}{\partial x^2}\right), \ \omega_{yx} = \frac{1}{2}\left(\frac{\partial \theta_y}{\partial y} + \frac{\partial^2 w}{\partial y^2}\right), \ \omega_{zx} = 0, \ \omega_{zy} = 0, \tag{3.9}$$

$$\omega_{xz} = \frac{1}{2}\left(\frac{\partial^2 v}{\partial x^2} - \frac{\partial^2 u}{\partial x \partial y} + z\frac{\partial^2 \theta_x}{\partial x \partial y} - z\frac{\partial^2 \theta_y}{\partial x^2}\right),$$

$$\omega_{yz} = \frac{1}{2}\left(-\frac{\partial^2 u}{\partial y^2} + \frac{\partial^2 v}{\partial x \partial y} + z\frac{\partial^2 \theta_x}{\partial y^2} - z\frac{\partial^2 \theta_y}{\partial x \partial y}\right);$$

$$\chi_x = \frac{1}{2}\left(\frac{\partial \theta_y}{\partial x} + \frac{\partial^2 w}{\partial x \partial y}\right), \quad \chi_y = \frac{1}{2}\left(-\frac{\partial^2 w}{\partial y \partial x} - \frac{\partial \theta_x}{\partial y}\right),$$

$$\chi_z = \frac{1}{2}\left(\frac{\partial \theta_x}{\partial y} - \frac{\partial \theta_y}{\partial x}\right),$$

$$\chi_{xy} = \chi_{yx} = \frac{1}{4}\left(-\frac{\partial \theta_x}{\partial x} - \frac{\partial^2 w}{\partial x^2} + \frac{\partial \theta_y}{\partial y} + \frac{\partial^2 w}{\partial y^2}\right), \tag{3.10}$$

$$\chi_{xz} = \chi_{zx} = \frac{1}{4}\left(\frac{\partial^2 v}{\partial x^2} - \frac{\partial^2 u}{\partial x \partial y} + z\frac{\partial^2 \theta_x}{\partial x \partial y} - z\frac{\partial^2 \theta_y}{\partial x^2}\right),$$

$$\chi_{yz} = \chi_{zy} = \frac{1}{4}\left(-\frac{\partial^2 u}{\partial y^2} + \frac{\partial^2 v}{\partial x \partial y} + z\frac{\partial^2 \theta_x}{\partial y^2} - z\frac{\partial^2 \theta_y}{\partial x \partial y}\right);$$

$$k_x = k_y = k_y = 0, \quad k_{xy} = -k_{yx} = \frac{1}{4}\left(-\frac{\partial \theta_x}{\partial x} - \frac{\partial^2 w}{\partial x^2} - \frac{\partial \theta_y}{\partial y} - \frac{\partial^2 w}{\partial y^2}\right),$$

$$k_{xz} = -k_{zx} = \frac{1}{4}\left(\frac{\partial^2 v}{\partial x^2} - \frac{\partial^2 u}{\partial x \partial y} + z\frac{\partial^2 \theta_x}{\partial x \partial y} - z\frac{\partial^2 \theta_y}{\partial x^2}\right), \tag{3.11}$$

$$k_{yz} = -k_{zy} = \frac{1}{4}\left(-\frac{\partial^2 u}{\partial y^2} + \frac{\partial^2 v}{\partial x \partial y} + z\frac{\partial^2 \theta_x}{\partial y^2} - z\frac{\partial^2 \theta_y}{\partial x \partial y}\right).$$

Equations (3.9) to (3.11) are linearized. In fact, it is assumed that the changes of $\left(\frac{\partial w}{\partial x}\right)^2$, $\left(\frac{\partial w}{\partial y}\right)^2$, and $\left(\frac{\partial w}{\partial x}\right)\left(\frac{\partial w}{\partial y}\right)$ with respect to x and y are insignificant, as a result, the terms $-2\partial\varepsilon_x^{NL}/\partial y + \partial\gamma_{xy}^{NL}/\partial x$ and $-\partial\gamma_{xy}^{NL}/\partial y + 2\partial\varepsilon_y^{NL}/\partial x$ are insignificant and therefore ignored. From this point of view, the strain is small, the rotation of the transverse normal is moderate, and the micro-curvature tensor $\hat{\Gamma} = \omega$ (and also its symmetric and antisymmetric parts, that is, the twist tensor χ and the mean curvature tensor k) is assumed to be small. It should be noted that available works in the literature have directly used the linear form of curvature without considering the mentioned linearization [54–56]. Equations (3.7)–(3.11) are issued in the orthogonal Cartesian coordinate system, however, the above-mentioned point can be easily achieved in the cylindrical coordinate system or other form of the orthogonal curvilinear coordinate system. Using Eq. (2.5), or alternatively Eq. (3.11) and considering $k_i = 1/2e_{ijk}k_{jk}$, the mean curvature vector is obtained as:

$$
\begin{aligned}
k_x &= -\frac{1}{4}\left(\frac{\partial^2 u}{\partial y^2} - \frac{\partial^2 v}{\partial x \partial y} + z\frac{\partial^2 \theta_y}{\partial x \partial y} - z\frac{\partial^2 \theta_x}{\partial y^2}\right),\\
k_y &= -\frac{1}{4}\left(\frac{\partial^2 v}{\partial x^2} - \frac{\partial^2 u}{\partial x \partial y} + z\frac{\partial^2 \theta_x}{\partial x \partial y} - z\frac{\partial^2 \theta_y}{\partial x^2}\right),\\
k_z &= -\frac{1}{4}\left(\frac{\partial^2 w}{\partial x^2} + \frac{\partial \theta_x}{\partial x} + \frac{\partial^2 w}{\partial y^2} + \frac{\partial \theta_y}{\partial y}\right),
\end{aligned}
\tag{3.12}
$$

which can be expressed as follows:

$$
k_b = k_z = -\frac{1}{4}\left(\frac{\partial^2 w}{\partial x^2} + \frac{\partial \theta_x}{\partial x} + \frac{\partial^2 w}{\partial y^2} + \frac{\partial \theta_y}{\partial y}\right),
\tag{3.13}
$$

$$
\begin{aligned}
k_s &= [k_x \; k_y]^T = k_s^0 + z k_s^1,\\
k_s^0 &= -\frac{1}{4}\left[\left(\frac{\partial^2 u}{\partial y^2} - \frac{\partial^2 v}{\partial x \partial y}\right) \;\; \left(\frac{\partial^2 v}{\partial x^2} - \frac{\partial^2 u}{\partial x \partial y}\right)\right]^T,\\
k_s^1 &= \frac{1}{4}\left[\left(\frac{\partial^2 \theta_x}{\partial y^2} - \frac{\partial^2 \theta_y}{\partial x \partial y}\right) \;\; \left(\frac{\partial^2 \theta_y}{\partial x^2} - \frac{\partial^2 \theta_x}{\partial x \partial y}\right)\right]^T.
\end{aligned}
\tag{3.14}
$$

As mentioned in the previous section, the bending deformation of the infinitesimal element is associated with the imposed micro-rotation ϕ, which is considered by the mean curvature tensor/vector under C-CST assumptions. In this respect, ellipsoidal cap-like deformation of surface elements is guaranteed (a positive Gaussian curvature), while this is not the case under twist tensor and MCST. As shown in Fig. 1, k_x, k_y, and k_z represent the mean curvature of planes parallel to the yz, xz, and xy planes, respectively. The mean curvature k_b is a constant value through the plate thickness, while k_s changes linearly.

The small deformation assumptions require the components of the macro-strain tensor and the mean curvature vector to be infinitesimal (i.e., $|\varepsilon_{ij}| \ll 1$ and $|k_i| \ll \frac{1}{\iota}$) [13]. The geometrical nonlinearity of plates can be treated in two ways, large-deflections and stability problems. In the aforementioned formulations, a general nonlinear expression was used to reveal that the von Karman nonlinear strain terms vanish in the curvature tensor. In the following, geometrical nonlinearity is retained for a buckling analysis. Concerning a linear elastic isotropic material enriched by couple stress effect, Eq. (2.6) reveals that the symmetric force-stress tensor is the energy conjugate of the symmetric macro-strain tensor, while the couple-stress vector is the energy conjugate of the true mean curvature vector. Therefore, the constitutive equations can be made of Eqs. (2.7), (3.4), and (3.5) as:

$$\begin{aligned} \sigma_b &= [\sigma_x \ \sigma_y \ \tau_{xy}]^T = Q_b \varepsilon_b, \\ \sigma_s &= [\tau_{yz} \ \tau_{xz}]^T = Q_s \varepsilon_s, \end{aligned} \tag{3.15}$$

$$Q_b = \frac{E}{1-\vartheta^2} \begin{bmatrix} 1 & \vartheta & 0 \\ \vartheta & 1 & 0 \\ 0 & 0 & \frac{1-\vartheta}{2} \end{bmatrix}, \quad Q_s = G \begin{bmatrix} 1 & 0 \\ 0 & 1 \end{bmatrix}, \tag{3.16}$$

where G is the shear modulus. The couple-stress vector μ can also be expressed as follows:

$$\begin{aligned} \mu_b &= \mu_z = -Q_{kb} k_b, \\ \mu_s &= [\mu_x \ \mu_y]^T = -Q_{ks} k_s, \end{aligned} \tag{3.17}$$

$$Q_{kb} = 8\eta, \quad Q_{ks} = \begin{bmatrix} 8\eta & 0 \\ 0 & 8\eta \end{bmatrix}. \tag{3.18}$$

3.2. A novel unified form for homogenization of FG-NC plate

In conventional functionally graded materials, composite properties including the modulus of elasticity, change continuously in predefined directions and are defined as a function of the primary values (see Fig. 2b) [57]. On the other hand, a conventional phased composite/nanocomposite usually includes one or more reinforcement parts that are surrounded by a continuous phase. As shown in Fig. 2b, the mechanical properties of phased composite are defined as a function of the separate properties of the matrix and reinforcement [58–60]. The gradual change of constituent material in the phased composites can lead to higher performance of the final product [58]. A review of the literature reveals that in most of the works dedicated to functionally graded composite/nanocomposite plates, the graded parameter is the volume fraction of the reinforcement phase [42]. However, gradual changes in the shape, size, orientation, and mechanical properties of the dispersed phase as well as the properties of the matrix material can

also be considered. From this point of view, using the Halpin–Tsai model [58–60] and a special grading function [57], a unified form will be constructed for the graphene-based functionally graded nanocomposite plate. A generic form of functionally graded pattern is as follows [57]:

$$P(z) = p_0 V(z), \tag{3.19}$$

where P denotes material properties such as Young's modulus E and mass density ρ. P_0 is an initial value at the origin surface. V can be written as [57]:

$$V_m(z) = \left(1 + \beta_m \left(\frac{1}{2} \pm \frac{z}{h}\right)\right)^{n_m}, \quad V_r(z) = \left(1 + \beta_r \left(\frac{1}{2} \pm \frac{z}{h}\right)\right)^{n_r}, \tag{3.20}$$

grading index β can be obtained as follows:

$$\beta_m = \sqrt[n_m]{P_m(h/2)/P_{m0}} - 1, \quad \beta_r = \sqrt[n_r]{P_r(h/2)/P_{r0}} - 1, \tag{3.21}$$

subscripts m and r denote dependence on matrix and reinforcement, respectively. n_m and n_r represent a predefined integer related to the matrix and reinforcement, respectively. Other FG forms include an exponential grading pattern that can be used [57]. Consider useful ratios as follows:

$$\alpha_V(z) = \frac{V_r(z)}{V_m(z)}, \quad \alpha_E = \frac{E_{r0}}{E_{m0}}, \quad \alpha_\rho = \frac{\rho_{r0}}{\rho_{m0}}. \tag{3.22}$$

Under Halpin and Tsai assumptions [58–60], the phased composite modulus is defined as a function of the matrix and reinforcement modulus along with the geometrical parameters of the dispersed phase, i.e., $\frac{p}{p_m} = \frac{1+\xi\eta\bar{V}_r}{1-\eta\bar{V}_r}$, where $\eta = \frac{p_r}{p_m} - 1/\frac{p_r}{p_m} + \xi\bar{V}_r$ and ξ are volume fraction and geometry parameter of reinforcement, respectively. In this respect, utilizing the Halpin–Tsai model, the ratio of in-plane modulus of the FG-NC reinforced by rectangular surface filler can be written in a unified form as follows:

$$\frac{E_\parallel(z)}{E_\perp(z)} = \frac{\alpha_L(z)\alpha_W(z) + \alpha(z)\alpha_{LW}(z)\bar{V}_r(z) - \alpha^2(z)\xi_L\bar{V}_r^2(z)}{\alpha_L(z)\alpha_W(z) + \alpha(z)\alpha_{WL}(z)\bar{V}_r(z) - \alpha^2(z)\xi_w\bar{V}_r^2(z)}, \tag{3.23}$$

$$\frac{E_\parallel(z)}{E_m(z)} = \frac{\alpha_L(z) + \xi_L\alpha(z)\bar{V}_r}{\alpha_L(z) - \alpha(z)\bar{V}_r}, \tag{3.24}$$

where $E_\parallel$ and $E_\perp$ are longitudinal and transverse Young's modulus, respectively. $\xi_L = 2L/3t$ and $\xi_w = 2W/3t$ are the filler geometric parameters. L, W and t are the length, width, and thickness of rectangular fillers. Alternatively, one can use geometrical parameters in the form of $\xi_L = 2((L+W)/2/t)$ and $\xi_w = 2$ [59, 61].

The pertinent parameters are defined as:

$$
\begin{aligned}
&\alpha_{LW}(z) = \alpha_W(z)\xi_L - \alpha_L(z), \quad \alpha_{WL}(z) = \alpha_L(z)\xi_w - \alpha_W(z),\\
&\alpha(z) = \alpha_E\alpha_V(z) - 1, \quad \alpha_L(z) = \alpha_E\alpha_V(z) + \xi_L,\\
&\alpha_W(z) = \alpha_E\alpha_V(z) + \xi_W,\\
&\bar{V}_r = \frac{\Lambda_r}{\Lambda_r + \alpha_\rho\alpha_V(z)(1-\Lambda_r)},
\end{aligned}
\tag{3.25}
$$

where Λ_r denotes the filler weight fraction. The Young modulus of the FG-NC plate is given by:

$$
E_{\text{random}}(z) = a_1E_{\parallel}(z) + a_2E_{\perp}(z), \tag{3.26}
$$

which reduces to the conventional FG plate by assuming $\Lambda_r = 0$. Coefficients a_1 and a_2 are $3/8$ and $5/8$ for the rectangular-surface filler. Also, these coefficients are given as 0.49 and 0.51 in [62] for the nonrectangular-surface GO. In this respect, geometrical parameters are $\xi_L = \xi_w = 2d/t$, where, d and t denote the average diameter and thickness of fillers. For the unidirectional (longitudinal) arranged filler $E_{\text{random}}(z) = E_{\parallel}(z)$. Similar grading of the filler and the matrix through the plate thickness (i.e., $n_m = n_r$ and $\beta_m = \beta_r$) results in $\alpha_V = 1$, which gives:

$$
E_{\text{random}}(z) = (a_1E_{\parallel} + a_2E_{\perp})V_m(z). \tag{3.27}
$$

The unified form can be reduced to the homogeneous model ($\Lambda_r = 0$, $\beta_m = 0$, $V_m(z) = 1$), conventional functionally graded model ($\Lambda_r = 0$), conventional reinforced nanocomposite ($\beta_m = \beta_r = 0$, $\bar{V}_r(z) = V_m(z) = V_r(z) = 1$), and conventional functionally graded reinforced nanocomposite ($\beta_m = \beta_r = 0$, $V_m(z) = V_r(z) = 1$). The mass density and Poisson's ratio of FG-NC plate are given by the rule of mixture as:

$$
\begin{aligned}
&\rho(z) = (\rho_r(z) - \rho_m(z))\bar{V}_r(z) + \rho_m(z),\\
&\nu(z) = (\nu_r(z) - \nu_m(z))\bar{V}_r(z) + \nu_m(z),
\end{aligned}
\tag{3.28}
$$

ν_r and ν_m are Poisson's ratio of the filler and the matrix, respectively. Dispersion patterns in the thickness direction are considered as:

$$
\bar{V}_r(z) = \bar{V}_r \qquad \text{(UD)}, \tag{3.29}
$$

$$
\bar{V}_r(z) = 2\bar{V}_r\left(\frac{h - 2|z|}{h}\right) \qquad \text{(OD)}, \tag{3.30}
$$

$$
\bar{V}_r(z) = 4\bar{V}_r\frac{|z|}{h} \qquad \text{(XD)}, \tag{3.31}
$$

$$
\bar{V}_r(z) = \bar{V}_r\left(\frac{h + 2z}{h}\right) \qquad \text{(VD)}. \tag{3.32}
$$

3.3. Weak form equations of Mindlin FG-NC plates

By using Eqs. (3.15) and (3.17), the CCST-based elastic energy (2.6) can be rewritten as:

$$U = \frac{1}{2}\int\limits_V \varepsilon_b^T Q_b \varepsilon_b \, dV + \frac{\kappa}{2}\int\limits_V \varepsilon_s^T Q_s \varepsilon_s \, dV + \int\limits_V k_b^T Q_{kb} k_b \, dV + \int\limits_V k_s^T Q_{ks} k_s \, dV, \tag{3.33}$$

where κ is the shear correction factor, and can be taken as $5/6$. Utilizing Eqs. (3.4), (3.5), (3.13), and (3.33), the first variation of U takes the following form:

$$\begin{aligned}\delta U = \int\limits_\Omega \Big(& \delta {\varepsilon_b^0}^T \Big[\int\limits_z Q_b \, dz\Big] \varepsilon_b^0 - \delta {\varepsilon_b^0}^T \Big[\int\limits_z z Q_b \, dz\Big] \varepsilon_b^1 - \delta {\varepsilon_b^1}^T \Big[\int\limits_z z Q_b \, dz\Big] \varepsilon_b^0 \\ & + \delta {\varepsilon_b^1}^T \Big[\int\limits_z z^2 Q_b \, dz\Big] \varepsilon_b^1 \, d\Omega + \int\limits_\Omega \delta \varepsilon_s^T \Big[\int\limits_z \kappa Q_s \, dz\Big] \varepsilon_s \, d\Omega \\ & + 2\int\limits_\Omega \delta k_b^T \Big[\int\limits_z Q_{kb} \, dz\Big] k_b \, d\Omega + 2\int\limits_\Omega \Big(\delta {k_s^0}^T \Big[\int\limits_z Q_{ks} \, dz\Big] k_s^0 \\ & + \delta {k_s^0}^T \Big[\int\limits_z z Q_{ks} \, dz\Big] k_s^1 + \delta {k_s^1}^T \Big[\int\limits_z z Q_{ks} \, dz\Big] k_s^0 \\ & + \delta {k_s^1}^T \Big[\int\limits_z z^2 Q_{ks} \, dz\Big] k_s^1 \Big) \, d\Omega,\end{aligned} \tag{3.34}$$

where Ω denotes the middle plane of the plate. The variational form of the kinetic energy of the FG-NC plate is defined as:

$$\begin{aligned}\delta T = & \int\limits_\Omega \Big(\delta \dot{w} \Big[\int\limits_z \rho \, dz\Big] \dot{w} + \delta \dot{\theta}_x \Big[\int\limits_z \rho z^2 \, dz\Big] \dot{\theta}_x + \delta \dot{\theta}_y \Big[\int\limits_z \rho z^2 \, dz\Big] \dot{\theta}_y \Big) \, d\Omega \\ & + \int\limits_\Omega \Big(\delta \dot{u} \Big[\int\limits_z \rho \, dz\Big] \dot{u} + \delta \dot{v} \Big[\int\limits_z \rho \, dz\Big] \dot{v} \Big) \, d\Omega \\ & - 2\int\limits_\Omega \Big(\delta \dot{u} \Big[\int\limits_z \rho z \, dz\Big] \dot{\theta}_x + \delta \dot{v} \Big[\int\limits_z \rho z \, dz\Big] \dot{\theta}_y \Big) \, d\Omega,\end{aligned} \tag{3.35}$$

the superposed dot denotes derivative with respect to time. To capture the geometrical nonlinearity of the elastic buckling, by using von Karman nonlinear strains (3.3), the potential of in-plane edge forces $N^0 = [N_x^0 \; N_y^0 \; N_{xy}^0]^T$ are expressed as follows:

$$\mathcal{V} = \int\limits_\Omega {N^0}^T \varepsilon^{NL} \, d\Omega, \tag{3.36}$$

the first variation gives:

$$\delta\mathcal{V} = \int\limits_{\Omega} \left(\frac{\partial \delta w}{\partial x} N_x^0 \frac{\partial w}{\partial x} + \frac{\partial \delta w}{\partial y} N_y^0 \frac{\partial w}{\partial y} + \frac{\partial \delta w}{\partial x} N_{xy}^0 \frac{\partial w}{\partial y} + \frac{\partial \delta w}{\partial y} N_{xy}^0 \frac{\partial w}{\partial x} \right) d\Omega, \tag{3.37}$$

the Hamilton principle in a weak form sense gives:

$$\int\limits_{\Omega} \left(\delta\bar{\varepsilon}_b^T D_b \bar{\varepsilon}_b + \delta\varepsilon_s^T D_s \varepsilon_s + \delta k_b^T D_{kb} k_b + \delta\bar{k}_s^T D_{ks} \bar{k}_s \right) d\Omega = \mathcal{A}, \tag{3.38}$$

where $\bar{\varepsilon}_b = [\varepsilon_b^0 \ \varepsilon_b^1]^T$, $\bar{k}_s = [k_s^0 \ k_s^1]^T$. Moreover, the relevant parameters are as follows:

$$\begin{gathered} D_b = \begin{bmatrix} D_b^0 & D_b^{01} \\ D_b^{01} & D_b^1 \end{bmatrix}, \quad (D_b^0, D_b^{01}, D_b^1) = \int\limits_{-h/2}^{h/2} (1, -z, z^2) Q_b \, dz, \\ D_s = \int\limits_{-h/2}^{h/2} \kappa Q_s \, dz, \quad D_{kb} = 2 \int\limits_{-h/2}^{h/2} Q_{kb} \, dz, \\ D_{ks} = \begin{bmatrix} D_{ks}^0 & D_{ks}^{01} \\ D_{ks}^{01} & D_{ks}^1 \end{bmatrix}, \quad (D_{ks}^0, D_{ks}^{01}, D_{ks}^1) = 2 \int\limits_{-h/2}^{h/2} (1, z, z^2) Q_{ks} \, dz, \end{gathered} \tag{3.39}$$

$\mathcal{A}$ for bending, free vibration, and buckling analysis of the plate defined as follows, respectively:

$$\mathcal{A}_{be} = \int\limits_{\Omega} p\delta w \, d\Omega + \int\limits_{\mathbb{S}} \bar{t}_z \delta w \, d\Gamma - \int\limits_{\mathbb{S}} \bar{m}_x \delta\theta_x \, d\Gamma - \int\limits_{\mathbb{S}} \bar{m}_y \delta\theta_y \, d\Gamma, \tag{3.40}$$

$$\mathcal{A}_{fv} = \int\limits_{\Omega} \delta\dot{\bar{u}}^T M \dot{\bar{u}} \, d\Omega, \tag{3.41}$$

$$\mathcal{A}_{bu} = \int\limits_{\Omega} [(\nabla \delta w^T N \nabla w] \, d\Omega, \tag{3.42}$$

where $\bar{u} = [u^0 \ u^1]$, $u^0 = [u \ v]$, $u^1 = [w \ \theta_x \ \theta_y]$. Moreover, the pertinent parameters defined as:

$$M = \begin{bmatrix} m_0 & 0 \\ 0 & M^1 \end{bmatrix}, \ M^1 = \begin{bmatrix} m_0 & 0 & 0 \\ 0 & m_2 & 0 \\ 0 & 0 & m_2 \end{bmatrix}, \ (m_0, m_2) = \int\limits_{-h/2}^{h/2} \rho(1, z^2) \, dz, \tag{3.43}$$

$$\nabla = \begin{bmatrix} \dfrac{\partial}{\partial x} & \dfrac{\partial}{\partial y} \end{bmatrix}^{\mathrm{T}}, \quad N = \begin{bmatrix} N_x^0 & N_{xy}^0 \\ N_{xy}^0 & N_y^0 \end{bmatrix}, \tag{3.44}$$

a parameter ρ denotes the density of the plate; $\mathbb{s}$ is the boundary of Ω. The parameter p is the transverse pressure; $\bar{t}_{\mathbf{z}}$ is force per unit length acting on the natural boundary $\mathbb{s}$. $\bar{m}_x$ and $\bar{m}_y$ are the applied moments per unit length about axes y and x acting on the boundary $\mathbb{s}$; N is the in-plane edge forces matrix.

4. Size-dependent finite element discretization

In this section, a size-dependent finite element based on C-CST is constructed for the FG-NC Mindlin plate theory. An important issue in the analysis of 2D problems based on the finite element method is that the weak solution must be a function of the Sobolev space $\mathrm{H}^2(\Omega)$, which in turn requires C^1 continuity for the ansatz since C^0 is not sufficient. CST requires C^1 continuity to ensure the integrability of the weak form. This is due to the existence of the second order derivatives of the translational displacements field in the curvature terms. C^1 continuity of primary variables guarantees that the secondary variables are piecewise continuous [63]. From this point of view, a very smooth function that guarantees a C^1 continuous element can be used. Hermitian elements are of interest due to their ability to provide C^1 interelement continuity. The degrees of freedom in Hermitian elements consist of the field variable and its derivatives. In this regard, the generalized displacements in a generic form can be independently interpolated using field functions and pertinent derivatives in the sense of Bognere–Foxe–Schmit (BFS) [64] as follows:

$$\hat{P} = \sum_{i=1}^{4} \left[N_i \hat{P}_i + N_{ix} \left(\frac{\partial \hat{P}}{\partial x} \right)_i + N_{iy} \left(\frac{\partial \hat{P}}{\partial y} \right)_i + N_{ixy} \left(\frac{\partial^2 \hat{P}}{\partial x \partial y} \right)_i \right], \tag{4.1}$$

where $\hat{P}$ denotes generalized displacements u, v, w, θ_x, and θ_y. This expression leads to 20-DOF per node (80-DOF 4-node element) which is reduced to 12-DOF per node in the case of bending modelling without stretching. $\hat{P}$ can be approximated by using the third order polynomial $a_1 + a_2 x + \cdots + a_{16} \mathrm{x}^3 \mathrm{y}^3$. $\hat{P}$ and its partial derivatives construct a system of equations as:

$$\hat{d} = Aa, \tag{4.2}$$

where $\hat{d} = [\hat{P}_1, \hat{P}_2, \hat{P}_3, \hat{P}_4, \hat{P}_{,x1}, \hat{P}_{,x2}, \hat{P}_{,x3}, \hat{P}_{,x4}, \hat{P}_{,y1}, \hat{P}_{,y2}, \hat{P}_{,y3}, \hat{P}_{,y4}, \hat{P}_{,xy1}, \hat{P}_{,xy2}, \hat{P}_{,xy3}, \hat{P}_{,xy4}]$, a_j is the coefficient vector $(j = 1, \ldots, 12)$, A is the matrix of coefficients, as a node location function in terms of natural coordinate $(\xi\eta)$. On the other hand, since C^1 continuity is difficult to satisfy, many works in the literature use elements that provide slope continuity only at the nodes and not along the element boundaries, which leads to the production of a nonconforming element. A non-conforming approximation in the sense of Adinie–Cloughe–Melosh

(ACM) [65] can be obtained by dropping partial derivatives $\partial^2/\partial x\partial y$, x^2y^2, x^3y^2, x^2y^3, and x^3y^3 terms, which produce 15-DOF at each node in the general case, and 9-DOF per node in bending form without stretching. Substituting $a = A^{-1}\hat{d}$ in the mentioned third order form $\hat{P}$ and by extracting all multiplied terms in $\hat{d}_j$, give:

$$
\begin{aligned}
N_i &= \frac{1}{16}(\xi+\xi_i)^2(\xi_0-2)(\eta+\eta_i)^2(\eta_0-2),\\
N_{ix} &= \frac{1}{16}a\xi_i(\xi+\xi_i)^2(1-\xi_0)(\eta+\eta_i)^2(\eta_0-2),\\
N_{iy} &= \frac{1}{16}b\eta_i(\xi+\xi_i)^2(\xi_0-2)(\eta+\eta_i)^2(1-\eta_0),\\
N_{ixy} &= \frac{1}{16}ab\xi_i\eta_i(\xi+\xi_i)^2(1-\xi_0)(\eta+\eta_i)^2(1-\eta_0),
\end{aligned}
\tag{4.3}
$$

where N_i, N_{ix}, N_{iy} and N_{ixy} identify shape functions, $\xi_0 = \xi\xi_i$, $\eta_0 = \eta\eta_i$ ($i = 1,2,3,4$), a and b are the half-length of the plate element. The finite element approximation of generalized displacements can be constructed in the matrix form as:

$$
U = \begin{bmatrix} w \\ \theta_x \\ \theta_y \end{bmatrix} = \hat{N}d^e, \qquad \bar{U} = \begin{bmatrix} u \\ v \end{bmatrix} = \bar{N}\bar{d}^e,
\tag{4.4}
$$

where

$$
d_i^e = \left[w_i\ \theta_{x_i}\ \theta_{y_i}\left(\frac{\partial w}{\partial x}\right)_i\left(\frac{\partial \theta_x}{\partial x}\right)_i\left(\frac{\partial \theta_y}{\partial x}\right)_i\left(\frac{\partial w}{\partial y}\right)_i\left(\frac{\partial \theta_x}{\partial y}\right)_i\left(\frac{\partial \theta_y}{\partial y}\right)_i\left(\frac{\partial^2 w}{\partial x\partial y}\right)_i\left(\frac{\partial^2 \theta_x}{\partial x\partial y}\right)_i\left(\frac{\partial^2 \theta_y}{\partial x\partial y}\right)_i\right]^{\mathrm{T}},
$$

d^e collects all the degrees of freedom of the generic element in the vector form, the superscript e denotes dependency on the element,

$$
\bar{d}_i^e = [u_i\ v_i\ u_{i,x}\ v_{i,x}\ u_{i,y}\ v_{i,y}\ u_{i,xy}\ v_{i,xy}]^T.
$$

Moreover, $\hat{N} = [\hat{N}_1 \dots \hat{N}_n]$ and $\bar{N} = [\bar{N}_1 \dots \bar{N}_n]$ are the matrix of the shape functions. $\hat{N}_i$ and $\bar{N}_i$ are expressed as follows:

$$
\hat{N}_i = \begin{bmatrix} N_i & 0 & 0 & N_{ix} & 0 & 0 & N_{iy} & 0 & 0 & N_{ixy} & 0 & 0 \\ 0 & N_i & 0 & 0 & N_{ix} & 0 & 0 & N_{iy} & 0 & 0 & N_{ixy} & 0 \\ 0 & 0 & N_i & 0 & 0 & N_{ix} & 0 & 0 & N_{iy} & 0 & 0 & N_{ixy} \end{bmatrix},
\tag{4.5}
$$

$$
\bar{N}_i = \begin{bmatrix} N_i & 0 & N_{ix} & 0 & N_{iy} & 0 & N_{ixy} & 0 \\ 0 & N_i & 0 & N_{ix} & 0 & N_{iy} & 0 & N_{ixy} \end{bmatrix}.
\tag{4.6}
$$

It should be noted that, under a sub-parametric manner, geometry mapping is performed by using a conventional Lagrangian interpolation scheme.

The strain vectors can be expressed based on pertinent differentiation of the shape functions ($\hat{N}$ and $\bar{N}$) along with the nodal displacements (d^e and $\bar{d}^e$) in the following form:

$$\varepsilon_b^0 = B_b^0 \bar{d}^e, \quad \varepsilon_b^1 = B_b^1 d^e, \quad \varepsilon_s = B_s d^e, \tag{4.7}$$

$$k_b = B_{kb} d^e, \quad k_s^0 = B_{ks}^0 \bar{d}^e, \quad k_s^1 = B_{ks}^1 d^e. \tag{4.8}$$

Utilizing Eqs. (4.4), (4.7), and (4.8), Eqs. (3.34), (3.35), and (3.37) can be written as:

$$\begin{aligned} \delta U = & \int_\Omega (\delta \bar{d}^{eT} {B_b^0}^T D_b^0 B_b^0 \bar{d}^e + \delta {d^e}^T {B_b^1}^T D_b^{01} B_b^0 \bar{d}^e \\ & + \delta \bar{d}^{eT} {B_b^0}^T D_b^{01} B_b^1 d^e + \delta {d^e}^T {B_b^1}^T D_b^1 B_b^1 d^e)\, d\Omega \\ & + \int_\Omega \delta {d^e}^T B_s^T D_s B_s d^e \, d\Omega + \int_\Omega \delta {d^e}^T B_{kb}^T D_{kb} B_{kb} d^e \, d\Omega \\ & + \int_\Omega (\delta \bar{d}^{eT} {B_{ks}^0}^T D_{ks}^0 B_{ks}^0 \bar{d}^e + \delta {d^e}^T {B_{ks}^1}^T D_{ks}^{01} B_{ks}^0 \bar{d}^e \\ & + \delta \bar{d}^{eT} {B_{ks}^0}^T D_{ks}^{01} B_{ks}^1 d^e + \delta {d^e}^T {B_{ks}^1}^T D_{ks}^1 B_{ks}^1 d^e)\, d\Omega, \end{aligned} \tag{4.9}$$

$$\delta T = \omega^2 e^{i\omega t} \int_\Omega \delta {d^e}^T \hat{N}^T M^1 \hat{N} d^e \, d\Omega + \omega^2 e^{i\omega t} \int_\Omega \delta \bar{d}^{eT} \bar{N}^T m_0 \bar{N} \bar{d}^e \, d\Omega, \tag{4.10}$$

$$\delta V = \int_\Omega \delta {d^e}^T \hat{N}^{WT} \nabla^{\mathrm{T}} N \nabla \hat{N}^W d^e \, d\Omega, \tag{4.11}$$

where ω is the natural frequency of a harmonic motion.

In this respect, the global equilibrium equations for bending, free vibration, and buckling can be respectively expressed as follows:

$$kd = F, \tag{4.12}$$

$$(k - \omega^2 M)d = \mathbf{0}, \tag{4.13}$$

$$(k - \lambda_{cr} k_g)d = \mathbf{0}, \tag{4.14}$$

where λ_{cr} denotes the load factor, $d = [d^e \ \bar{d}^e]^T$. The global stiffness matrix k, mass matrix M, force vector F, and geometrical stiffness matrix k_g can be written as follows:

$$k = \begin{bmatrix} \hat{k} & \tilde{k} \\ \tilde{k}^T & \bar{k} \end{bmatrix}, \tag{4.15}$$

$$F = \begin{bmatrix} f \\ 0 \end{bmatrix}, \tag{4.16}$$

$$M = \begin{bmatrix} \hat{M} & 0 \\ 0 & \bar{M} \end{bmatrix}, \tag{4.17}$$

$$k_g = \begin{bmatrix} k_g^1 & 0 \\ 0 & 0 \end{bmatrix}. \tag{4.18}$$

Equation (4.15) shows that the total stiffness matrix is affected by two main parts, the stiffness matrices representing the macro-translational degrees of freedom (k_b, k_s) and the stiffness matrices representing the micro-rotational degrees of freedom (k_{kb}, k_{ks}). This shows that adding the micro degree of freedom leads to an increase in global stiffness, reduces deflection and increases the frequency and critical load. Equation (4.14) can be expressed as $\overline{\overline{k}} - \lambda_{cr} I = \mathbf{0}$, where $\overline{\overline{k}} = (k_g^1)^{-1}\hat{k}$, I denotes the identity matrix. The lowest eigenvalue, at which bifurcation arises, can be reached by an iterative eigenvalue algorithm. To implement the presented method a computer code has been written in MATLAB environment. A system of Eqs. (4.12)–(4.14) using Eqs. (4.15)–(4.18) provides a decoupled form for in-plane and out-of-plane displacements as well as rotations. In this sense, $w\theta_x$, and θ_y can be independently determined based on certain initial and boundary conditions.

5. Size-dependent optimization of FG-NC plate model

The small-scale behaviour of the FG-NC plate is strongly dependent on the length scale parameter-to-thickness ratio $\Delta_l = \iota/h$. Therefore, to have optimal behaviour of the plate, it seems necessary to adjust the parameters of the FG-NC plate such as the weight fraction of dispersed phase Λ_r, grading index β, and length/width-to-thickness ratio n_a against Δ_l. In this respect, an optimization problem for minimizing plate weight can be defined as follows:

$$\begin{aligned} &\text{Minimize mass}(\Delta_l, \Lambda_r, \beta, n_a) = \rho n_a^2 \left(\frac{\iota}{\Delta_l}\right)^3, \\ &\text{subject to } 1 - R_\omega \leqslant 0, \\ &0.01 \leq \Delta_l \leq 1, \\ &0.001 \leq \Lambda_r \leq 0.02, \\ &0.1 \leq \beta \leq 2, \\ &5 \leq n_a \leq 100, \end{aligned} \tag{5.1}$$

where $R_\omega = \omega_1/\omega_1^a$, ω_1 denotes the first frequency of the plate, ω_1^a stands for the predefined lower bound of ω_1, which will be adopted by the designer. To solve the optimization problem, a computer code is written in the MATLAB environment based on a nonlinear program solver.

6. Numerical examples and discussion

In this section, numerical results are provided by the presented method for bending, frequency, and buckling analysis of FG-NC plates. The length scale parameter ι is assumed to be equal to 17.6 µm [66], also $n_r = n_m$, $\beta_r = \beta_m$ unless otherwise clearly expressed. As mentioned earlier, the C-CST elastic energy comparable to M-CST can be obtained by scaling $\eta \to \eta/4$ or $\iota \to \iota/2$. The properties of G are assumed $E_r = 1010\,\mathrm{GPa}$, $\rho_r = 1060\,\mathrm{kg/m^3}$, $\nu_r = 0.186$ [28, 51, 67], for GO $E_r = 290\,\mathrm{GPa}$, $\rho_r = 3600\,\mathrm{kg/m^3}$, $\nu_r = 0.179$ (for the degree of oxidation 0.06) [28, 67–69] for rGO under thermal reduction $E_r = 150\,\mathrm{GPa}$, $\rho_r = 2250\,\mathrm{kg/m^3}$, $\nu_r = 0.165$ [28, 51, 67], and for Ag/rGO with $E_{Ag} = 76\,\mathrm{GPa}$, $\rho_{\mathrm{Ag}} = 1049\,\mathrm{kg/m^3}$, $\nu_{\mathrm{Ag}} = 0.37$ [70] properties are $E_r = 147\,\mathrm{GPa}$, $\rho_r = 2225\,\mathrm{kg/m^3}$, $\nu_r = 0.169$. In addition, for the polymer matrix $E_m = 3\,\mathrm{GPa}$, $\rho_m = 1200\,\mathrm{kg/m^3}$, $\nu_m = 0.34$ [51, 70], for the CU matrix $E_m = 124\,\mathrm{GPa}$, $\rho_m = 8960\,\mathrm{kg/m^3}$, $\nu_m = 0.34$ [70]. The geometrical properties of graphene-based fillers can vary depending on the chemical composition and number of layers. In this respect, the length/width (L/W) of the fillers are considered in the range of 1 to 5 µm, and thicknesses are in the range of 1 to 5 nm [27, 28]. Various combinations of boundary conditions of simply (S), clumped (C), and free (F) support including SSSS, CCCC, SCSC, and CCCF are considered. Simply and clumped edge conditions are as follows:

Simply Supported Edge (S):

$$\begin{aligned} &\mathrm{v} = \mathrm{w} = \theta_y = 0 \quad \text{at } x = 0, a, \\ &\mathrm{u} = \mathrm{w} = \theta_x = 0 \quad \text{at } y = 0, b. \end{aligned}$$

Clamped Edge (C):

$$\begin{aligned} &\mathrm{u} = \mathrm{v} = w = w_{,y} = \theta_x = \theta_y = \theta_{x,y} = \theta_{y,y} = 0 \quad \text{at } x = 0, a, \\ &\mathrm{u} = \mathrm{v} = w = w_{,x} = \theta_x = \theta_y = \theta_{x,x} = \theta_{y,x} = 0 \quad \text{at } y = 0, b. \end{aligned}$$

6.1. Convergence study

Consider a homogeneous C-CST-based plate. Non-dimensional central deflections of the simply supported square plate under the sinusoidal load $p = p_0 \sin(\pi x/a) \sin(\pi y/b)$ and non-dimensional natural frequencies are tabulated in Table 1 for various material length scale parameter to thickness ratio ι/h and length to thickness ratio $a/h = 10$. Material properties are $E_m = 380\,\mathrm{GPa}$, $\rho_m = 3800\,\mathrm{kg/m^3}$, $\nu_m = 0.3$. Different meshes are captured to verify the convergence of the present method. As the results show, proper convergence can be achieved by employing 30×30 mesh, so that the difference in results with 40×40 mesh is about 0.1% or less in most cases. Therefore, a 30×30 mesh is used in

TABLE 1. Convergence of non-dimensional central deflection $\bar{w} = 10w\left(\frac{a}{2}, \frac{b}{2}, 0\right)E_m h^3/p_0 a^4$ and non-dimensional frequency $\bar{\omega} = \omega(a^2/h)\sqrt{\rho_m/E_m}$ of the plate, $\beta = 0$, $\Lambda_r = 0$, $\iota = 8.8\,\mu m$, $a = b = 10h$, SSSS.

Parameter	ι/h	Mesh						
		4×4	8×8	12×12	16×16	20×20	30×30	40×40
$\bar{w}$	0.1	0.2127	0.2438	0.2494	0.2513	0.2521	0.2529	0.2532
	0.2	0.1411	0.1679	0.1733	0.1752	0.1760	0.1768	0.1771
	0.3	0.0921	0.1116	0.1157	0.1171	0.1178	0.1185	0.1187
	0.4	0.0630	0.0766	0.0797	0.0807	0.0812	0.0817	0.0819
	0.5	0.0459	0.0552	0.0574	0.0582	0.0586	0.0590	0.0591
$\bar{\omega}$	0.1	5.7426	6.1062	6.1730	6.1983	6.2108	6.2240	6.2289
	0.2	7.0719	7.3675	7.4108	7.4281	7.4368	7.4462	7.4496
	0.3	8.7208	9.0442	9.0742	9.0866	9.0930	9.0998	9.1021
	0.4	10.4533	10.9173	10.9415	10.9513	10.9562	10.9612	10.9625
	0.5	12.1187	12.8660	12.8899	12.8987	12.9028	12.9067	12.9072

the following problems. In addition, in-plane displacements u and v are ignored in the following for convenience. As a result, the 48-DOF element is considered.

6.2. Static analysis

Table 2 gives results for the non-dimensional central deflection of the homogeneous square plate under a sinusoidal load for various length-to-thickness ratios a/h and material length scale parameter-to-thickness ratio ι/h. Material properties are $E_m = 380\,\text{GPa}$, $\rho_m = 3800\,\text{kg/m}^3$, $\nu_m = 0.3$.

The results show that the non-dimensional central deflection

$$\bar{w} = 10wE_m h^3/q_0 a^4$$

under the sinusoidal load has an inverse relation with the length-to-thickness ratio and the material length scale parameter-to-thickness, so non-dimensional deflection decreases with the increase of these two ratios. A comparison of the presented results with the other works including M-CST/C-CST based classical plate theory (CPT), the first-order shear deformation plate theory (FSDT), refined shear deformation plate theory (RSDT), and analytical/numerical 3D solutions shows a good agreement between data, especially with 3D C-CST, and when the length-to-thickness ratio increases. However, by increasing the material length scale parameter-to-thickness ratio and for the small length-to-thickness ratio (i.e., thicker plate), the difference between the 3D results and the plate theory data increases. As can be seen in Table 2, the presented element concerning the shear-locking phenomenon can provide accurate results for any length-to-thickness ratio without any need for reduced integration. This means that the full integration (e.g., 2×2 Gauss points) can be used in all cases.

Table 2. Non-dimensional central deflection $\bar{w} = 10w\left(\frac{a}{2}, \frac{b}{2}, 0\right)E_m h^3/q_0 a^4$ of the plate, $\beta = 0$, $\Lambda_r = 0$, $\iota = 8.8\,\mu\text{m}$, $a = b$, SSSS.

a/h	Theories	ι/h				
		0	0.1	0.25	0.4	0.5
5	M-CST CPT [71]	0.2803	0.2399	–	0.0760	0.0539
	M-CST RSDT [72]	0.3433	0.2875	–	0.0838	0.0588
	M-CST 3D [73]	0.3357	0.2851	–	0.0953	0.0709
	CCST 3D [47]	0.3357	0.2851	–	0.0953	0.0709
	Present	0.3411	0.2926	0.1690	0.0994	0.0746
10	M-CST RSDT [72]	0.2961	0.2520	–	0.0780	0.0552
	M-CST 3D [73]	0.2942	0.2514	–	0.0810	0.0583
	C-CST CPT [43]	0.2803	0.2310	0.1367	–	0.0539
	C-CST FSDT [43]	0.2961	0.2535	0.1454	–	0.0594
	C-CST RSDT [43]	0.2961	0.2520	0.1415	–	0.0551
	C-CST 3D [47]	0.2942	0.2514	–	0.0810	0.0583
	Present	0.2945	0.2529	0.1446	0.0817	0.0590
20	M-CST CPT [71]	0.2803	0.2399	–	0.0760	0.0539
	M-CST RSDT [72]	0.2842	0.2430	–	0.0765	0.0542
	M-CST 3D [73]	0.2838	0.2428	–	0.0773	0.0550
	CCST 3D [47]	0.2838	0.2428	–	0.0773	0.0550
	Present	0.2828	0.2428	0.1383	0.0772	0.0550
100	M-CST CPT [71]	0.2803	0.2399	–	0.0760	0.0539
	M-CST RSDT [72]	0.2804	0.2401	–	0.0760	0.0539
	Present	0.2791	0.2396	0.1363	0.0757	0.0537

The effects of dispersion patterns on the static behaviour of rGO-Epoxy FG-NC plate with $\Lambda_r = 1\%$, $L_r = W_r = 1\,\mu\text{m}$, $t_r = 1\,\text{nm}$ under concentrated force $p_0 = 0.1N$ at the centre are investigated in Table 3. Various non-homogeneity parameters β, width-to-length ratio b/a, length-to-thickness ratio a/h, and boundary conditions are considered. The central deflections $\bar{w}$ are provided for $\iota/h = 0.5$, $n = 2$. The obtained results show that the central deflection $\bar{w} = w/h$ of the plate has a direct relation with the length-to-thickness ratio a/h as well as the width-to-length ratio b/a, and an inverse relation with the grading index β. In the non-dimensional form of deflection in Tables 1 and 2, the relation between deflection and ι/h is inverse, while this relation is direct in Table 3. This is due to the thickness parameter h decreasing with the increase of ι/h when the material length scale parameter ι is considered a constant value. In fact, the thickness parameter h is in the numerator in Tables 1 and 2, while there is h in the denominator in Table 3. Interestingly, the presence of a dispersed phase leads to a significant decrease in the deflection. In this respect, by adding only 1% of rGO, the deflection will decrease by 20% and 22% for $\beta = 0$

TABLE 3. Central deflection $\bar{w} = w\left(\frac{a}{2}, \frac{b}{2}, 0\right)/h$ of the rGO-Epoxy FG-NC plate, $\Lambda_r = 1\%$, $L_r = W_r = 1\,\mu\text{m}$, $t_r = 1\,\text{nm}$, $\iota = 8.8\,\mu\text{m}$, $\iota/h = 0.5$.

B.C.	Dispersion pattern	b/a	$a/h = 10$			$a/h = 100$		
			$\beta = 0$	$\beta = 0.5$	$\beta = 1$	$\beta = 0$	$\beta = 0.5$	$\beta = 1$
SSSS	Pure Epoxy	0.5	0.1420	0.0896	0.0607	9.5895	6.0439	4.0867
		1	0.3242	0.2044	0.1384	26.8009	16.8914	11.4209
		1.5	0.4125	0.2601	0.1760	35.3891	22.3040	15.0805
	UD	0.5	0.1140	0.0719	0.0487	7.7010	4.8537	3.2819
		1	0.2603	0.1642	0.1111	21.5231	13.5650	9.1719
		1.5	0.3312	0.2089	0.1414	28.4200	17.9118	12.1108
	OD	0.5	0.1151	0.0727	0.0494	7.8527	4.9562	3.3591
		1	0.2640	0.1667	0.1131	21.9514	13.8541	9.3895
		1.5	0.3362	0.2123	0.1440	28.9868	18.2943	12.3987
	XD	0.5	0.1130	0.0712	0.0481	7.5545	4.7550	3.2079
		1	0.2568	0.1617	0.1092	21.1093	13.2866	8.9633
		1.5	0.3264	0.2056	0.1388	27.8725	17.5434	11.8349
	VD	0.5	0.1140	0.0700	0.0466	7.7001	4.7124	3.1297
		1	0.2603	0.1596	0.1061	21.5221	13.1695	8.7459
		1.5	0.3312	0.2030	0.1350	28.4187	17.3894	11.5482
CCCC	Pure Epoxy	0.5	0.0885	0.0558	0.0379	4.2330	2.6681	1.8043
		1	0.1874	0.1182	0.0801	12.9068	8.1348	5.5004
		1.5	0.2237	0.1411	0.0956	16.1611	10.1857	6.8871
	UD	0.5	0.0710	0.0448	0.0304	3.3995	2.1427	1.4489
		1	0.1504	0.0949	0.0623	10.3651	6.5228	4.4173
		1.5	0.1796	0.1133	0.0767	12.9785	8.1799	5.5309
	OD	0.5	0.0714	0.0451	0.0307	3.4647	2.1868	1.4823
		1	0.1519	0.0960	0.0652	10.5692	6.6706	4.5211
		1.5	0.1816	0.1147	0.0779	13.2348	8.3529	5.6613
	XD	0.5	0.0707	0.0446	0.0302	3.3364	2.1002	1.4170
		1	0.1490	0.0939	0.0635	10.1679	6.4000	4.3177
		1.5	0.1778	0.1120	0.0757	12.7309	8.0132	5.4060
	VD	0.5	0.0710	0.0437	0.0291	3.3993	2.0805	1.3819
		1	0.1504	0.0923	0.0615	10.3646	6.3426	4.2124
		1.5	0.1796	0.1102	0.0734	12.9779	7.9416	5.2743

and $\beta \neq 0$ cases, respectively. Besides, dispersion patterns VD and OD have the most and least effects, respectively. It should be noted that, when the homogeneity parameter β is ignored, the XD dispersed pattern gives the greatest effect.

Table 4 gives the non-dimensional central deflection of the square plate under concentrated force $p_0 = 0.1N$ at the centre with $a = b = 10h$ for the various material length scale parameter to thickness ratio ι/h, boundary conditions, and the filler/matrix type. Filler dimensions are $L_r = 2.5\,\mu\text{m}$, $W_r = 1.5\,\mu\text{m}$, $t_r = 1.5\,\text{nm}$ for G, and $L_r = W_r = 1\,\mu\text{m}$, $t_r = 1\,\text{nm}$ for GO, rGO, and Ag/rGO. According to the presented results, the presence of dispersed phase G and GO in

Table 4. Central deflection $\bar{w} = w\left(\frac{a}{2}, \frac{b}{2}, 0\right)/h$ of the NC plate, $\Lambda_r = 1\%$, $\beta = 0$, $a = b = 10h$, UD.

B.C.	Matrix	Filler	ι/h					
			0.05	0.2	0.4	0.6	0.8	1
SSSS	Pure Epoxy		3747e-6	3712e-5	7061e-5	8967e-5	1051e-4	1208e-4
	Epoxy	G	1019e-6	1009e-5	1917e-5	2434e-5	2852e-5	3278e-5
		GO	2926e-6	2898e-6	5512e-5	6998e-5	8202e-5	9425e-5
		rGO	3012e-6	2982e-5	5671e-5	7200e-5	8438e-5	9697e-5
		Ag/rGO	3017e-6	2987e-5	5680e-5	7211e-5	8452e-5	9712e-5
	Pure CU		9065e-8	8981e-7	1708e-6	2169e-6	2543e-6	2921e-6
	CU	G	5855e-8	5767e-7	1091e-6	1383e-6	1619e-6	1861e-6
		GO	8795e-8	8697e-7	1651e-6	2095e-6	2455e-6	2822e-6
		rGO	9022e-8	8910e-7	1690e-6	2143e-6	2511e-6	2885e-6
		Ag/rGO	9030e-8	8917e-7	1691e-6	2145e-6	2513e-6	2888e-6
CCCC	Pure Epoxy		2109e-6	2046e-5	3987e-5	5324e-5	6613e-5	8044e-5
	Epoxy	G	5734e-7	5557e-6	1082e-5	1445e-5	1795e-5	2183e-5
		GO	1647e-6	1597e-5	3112e-5	4155e-5	5161e-5	6278e-5
		rGO	1695e-6	1643e-5	3202e-5	4275e-5	5310e-5	6459e-5
		Ag/rGO	1698e-6	1646e-5	3207e-5	4282e-5	5318e-5	6469e-5
	Pure CU		5103e-8	4949e-7	9647e-7	1288e-6	1600e-6	1946e-6
	CU	G	3288e-8	3173e-7	6155e-7	8205e-7	1019e-6	1239e-6
		GO	4947e-8	4790e-7	9321e-7	1244e-6	1545e-6	1879e-6
		rGO	5072e-8	4905e-7	9535e-7	1272e-6	1578e-6	1922e-6
		Ag/rGO	5076e-8	4910e-7	9544e-7	1273e-6	1581e-6	1923e-6

the epoxy matrix reduce the deflection $\bar{w} = w/h$ by 73% and 22%, respectively, while for rGO and Ag/rGO, deflection reaches about 20 %. These effects in the copper matrix are equal to 35%, 3%, 1.2%, and 1% for G, GO, rGO, and Ag/rGO, respectively, which is to be expected, due to the higher mechanical properties of copper. The reduction of the oxidized form effect (also modified versions of graphene) is noticeable compared to the original graphene.

Instead, some critical issues such as agglomeration, interface bonding, and structural defects in the upgraded version of graphene are significantly less than graphene. Thus, the reduction of the critical issues concerning the fabrication procedure leads to the accurate results of the analytical model in accordance with the experimental results.

The results also are illustrated in Fig. 3. Figure 3a shows central deflection $\bar{w} = w\left(\frac{a}{2}, \frac{b}{2}, 0\right)/h$ in the form of $\bar{w}_{\text{Ag/rGO-Epoxy}}/\bar{w}_{\text{Epoxy}}$ versus the material length scale parameter-to-thickness ratio ι/h for various dispersion patterns. As can be seen in Fig. 3a, XD and OD patterns have the greatest and least effects on NC plate deflection, respectively. However, with the increase of the material length scale parameter-to-thickness ratio, the results of the four patterns converge with

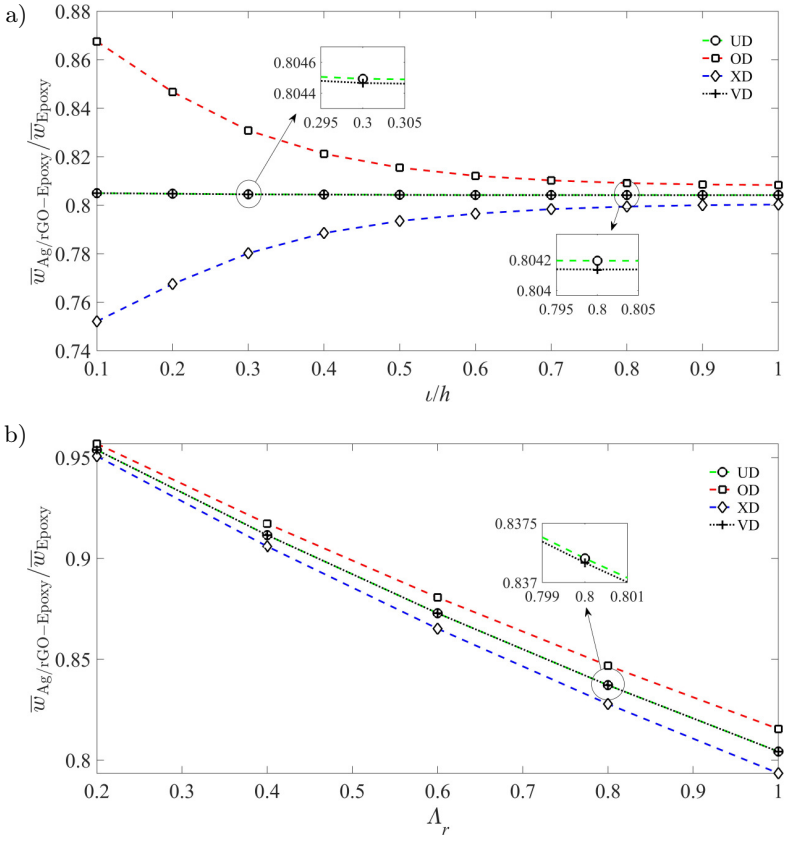

FIG. 3. Effect of various parameters on the deflection of NC plates under concentrated force: a) central deflection ratio $\bar{w}_{\mathrm{Ag/rGO\text{-}Epoxy}}/\bar{w}_{\mathrm{Epoxy}}$ versus material length scale parameter to thickness ratio ι/h with $\Lambda_r = 1\%$, b) central deflection ratio $\bar{w}_{\mathrm{Ag/rGO\text{-}Epoxy}}/\bar{w}_{\mathrm{Epoxy}}$ versus weight fraction Λ_r with $\iota/h = 0.5$ ($\bar{w} = w/h$, $\beta = 0$, $L_r = W_r = 1\,\mu\mathrm{m}$, $t_r = 1\,\mathrm{nm}$, $a = b = 10\,\mathrm{h}$, SSSS).

each other. In fact, when the small-scale effect becomes noticeable, there is no significant difference between various dispersion patterns concerning bending deflection. Figure 3b depicts the central deflection ratio $\bar{w}_{\mathrm{Ag/rGO\text{-}Epoxy}}/\bar{w}_{\mathrm{Epoxy}}$ versus weight fraction Λ_r for various dispersion patterns. As expected, increasing the filler weight fraction up to 1% leads to an impressive decrease in NC plate deflection, which is the most severe decrease in the XD pattern.

In Table 5 non-dimensional central deflections of the square Ag/rGO-Epoxy NC plate under the concentrated load 0.1 N at centre, uniform distributed load with intensity $P_0 = 3.23 \times 10^6(\iota/h)^2\,\mathrm{N/m^2}$, and sinusoidal distributed load with $P_0 = 7.97 \times 10^6(\iota/h)^2\,\mathrm{N/m^2}$ for the various material length scale parameter to thickness ratio ι/h are investigated.

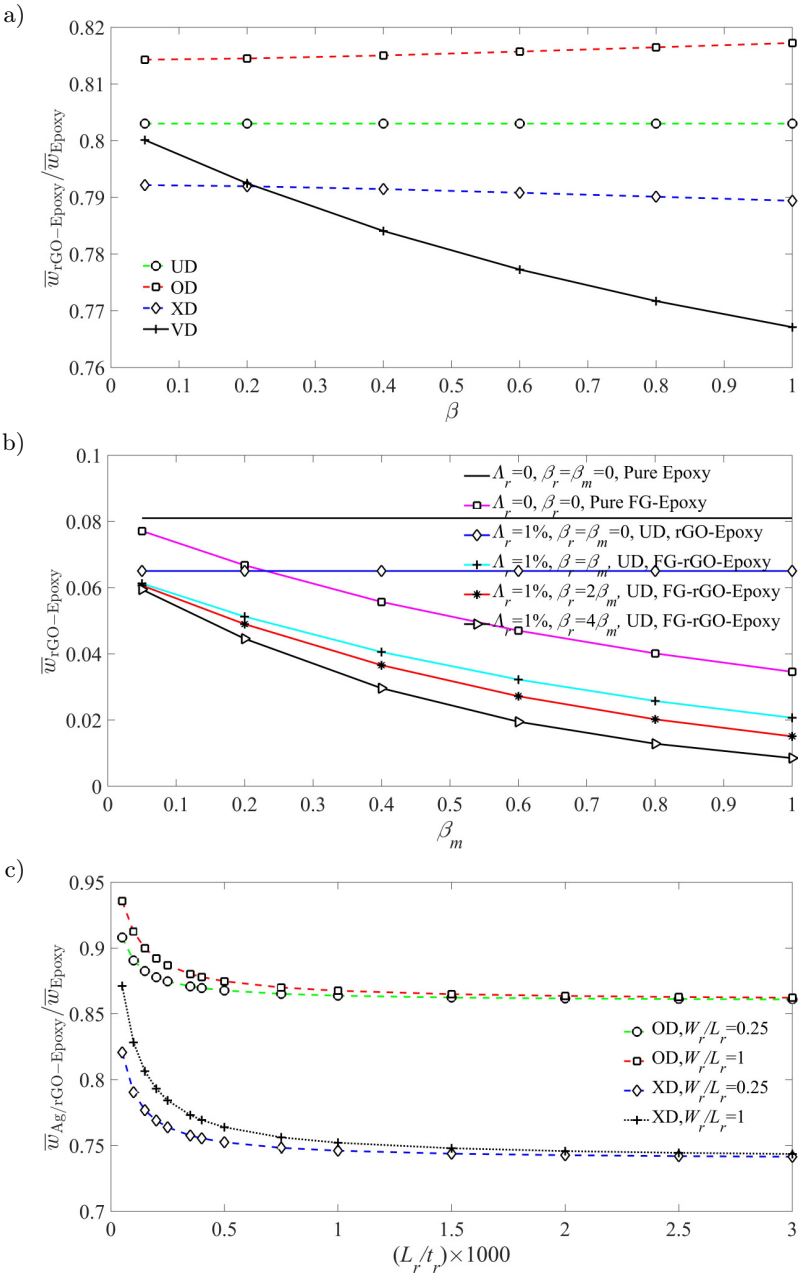

Fig. 4. Effect of various parameters on the deflection of NC plates under concentrated force: a) central deflection ratio $\bar{w}_{\text{rGO-Epoxy}}/\bar{w}_{\text{Epoxy}}$ versus grading index β with $\iota/h = 0.5$, b) central deflection $\bar{w}_{\text{rGO-Epoxy}}$ versus β_m, c) central deflection ratio $\bar{w}_{\text{Ag/rGO-Epoxy}}/\bar{w}_{\text{Epoxy}}$ versus L_r/t_r for various W_r/L_r with $\iota/h = 0.1$ ($\bar{w} = w/h$, $\Lambda_r = 1\%$, $n_r = n_m = 2$, $L_r = W_r = 1\,\mu\text{m}$, $t_r = 1\,\text{nm}$, $a = b = 10h$, SSSS).

TABLE 5. Central deflection $\bar{w} = w\left(\frac{a}{2}, \frac{b}{2}, 0\right)/h$ of the Ag/rGO-Epoxy NC plate, $\beta = 0$, $\Lambda_r = 1\%$, UD, $L_r = W_r = 1\,\mu\text{m}$, $t_r = 1\,\text{nm}$, $a = b = 10h$.

Load	B.C.	ι/h					
		0.05	0.2	0.4	0.6	0.8	1
Concentrated	SSSS	3017e-6	2987e-5	5680e-5	7211e-5	8452e-5	9712e-5
	CCCC	1698e-6	1646e-5	3207e-5	4282e-5	5318e-5	6469e-5
	SCSC	2036e-6	1991e-5	3858e-5	5089e-5	6235e-5	7485e-5
	CCCF	1928e-6	1881e-5	3686e-5	4946e-5	6161e-5	7499e-5
Uniform distributed	SSSS	9490e-7	9653e-6	1815e-5	2234e-5	2517e-5	2772e-5
	CCCC	3316e-7	3369e-6	6539e-6	8531e-6	1032e-5	1225e-5
	SCSC	4875e-7	4958e-6	9551e-6	1228e-5	1461e-5	1704e-5
	CCCF	4826e-7	4984e-6	1015e-5	1394e-5	1753e-5	2135e-5
Sinusoidal distributed	SSSS	1482e-6	1509e-5	2842e-5	3507e-5	3966e-5	4386e-5
	CCCC	5855e-7	5961e-6	1157e-5	1507e-5	1820e-5	2158e-5
	SCSC	8139e-7	8289e-6	1597e-5	2055e-5	2445e-5	2853e-5
	CCCF	7719e-7	7915e-6	1579e-5	2122e-5	2627e-5	3165e-5

The effect of the grading index β on FG-NC plate deflection is shown in Figs. 4a and 4b. Central deflection ratios $\bar{w}_{\text{rGO-Epoxy}}/\bar{w}_{\text{Epoxy}}$ of the NC plate for various dispersion patterns are presented. Interestingly, with the increase of the grading index (greater than 0.2), pattern VD takes the place of the pattern XD as the most effective dispersion scheme in reducing deflection. Figure 4b illustrates the effect of filler dimensions on the NC plate deflection.

6.3. Free vibration analysis

Table 6 gives results for the non-dimensional natural frequency of a simply supported homogeneous square plate for various length-to-thickness ratios a/h and material length scale parameter-to-thickness ratio ι/h. Material properties are $E_m = 14.4\,\text{GPa}$, $\rho_m = 12200\,\text{kg/m}^3$, $\nu_m = 0.38$. The material length scale parameter ι is considered equal to $8.8\,\mu\text{m}$. $\bar{m}$, $\bar{n}$ are the vibrational half-waves number of plates in the directions x and y, respectively. The results show that non-dimensional natural frequency $\bar{\omega} = \omega(a^2/h)\sqrt{\rho_m/E_m}$ has an inverse relation with the length-to-thickness ratio a/h and a direct relation with the material length scale parameter-to-thickness ratio ι/h, so non-dimensional natural frequency decreases/increases with the increase of length-to-thickness ratio/material length scale parameter-to-thickness ratio. Comparing present results with the other works including M-CST/C-CST-based classical plate theory (CPT) and the first-order shear deformation plate theory (FSDT) shows a good agreement between data.

Table 6. Non-dimensional natural frequency $\bar{\omega} = \omega(a^2/h)\sqrt{\rho_m/E_m}$ of plate, $\beta = 0$, $\Lambda_r = 0$, $\iota = 8.8\,\mu\text{m}$, $a = b$, SSSS.

a/h	Theories	$\bar{m}=1,\ \bar{n}=1$			$\bar{m}=1,\ \bar{n}=2$		
		$\iota=0$	$\iota/h=0.2$	$\iota/h=0.4$	$\iota=0$	$\iota/h=0.2$	$\iota/h=0.4$
5	M-CST CPT [74]	5.9671	7.5366	10.9718	14.2717	18.0253	24.2521
	M-CST FSDT [74]	5.3871	6.7996	9.6451	11.6717	14.8649	20.8542
	Present	5.3855	6.8078	9.6698	11.6514	14.8924	20.8856
10	C-CST CPT [43]	6.1103	7.7174	11.2349	15.0936	19.0634	27.7525
	C-CST FSDT [43]	5.9301	7.4807	10.7848	14.0893	17.7680	25.3657
	Present	5.9292	7.4776	10.7931	14.0802	17.7733	25.3958
20	M-CST CPT [74]	6.1477	7.7646	11.3037	15.3223	19.3522	28.1730
	M-CST FSDT [74]	6.0997	7.7009	11.1801	15.0319	18.9688	27.4365
	Present	6.0991	7.6945	11.1794	15.0268	18.9618	27.4431

In Table 7, the non-dimensional natural frequencies $\bar{\omega} = \omega h\sqrt{\rho_m/E_m}$ of the rGO-Epoxy NC plate are presented for various length-to-thickness ratio a/h, dispersion patterns, mode number, and boundary conditions. The rGO properties are considered $E_r = 250\,\text{GPa}$, $\rho_r = 2250\,\text{kg/m}^3$, $\nu_r = 0.165$, $L_r = W_r = 1\,\mu\text{m}$, $t_r = 1\,\text{nm}$ [51]. The results reveal that the largest and lowest values for natural

Table 7. Non-dimensional natural frequency $\bar{\omega} = \omega h\sqrt{\rho_m/E_m}$ of rGO-Epoxy NC plate, $\Lambda_r = 1\%$, $L_r = W_r = 1\,\mu\text{m}$, $t_r = 1\,\text{nm}$ $\beta = 0$, $\iota = 0$, $a = b$.

B.C.	Dispersion pattern	Method	$\bar{m}=1,\ \bar{n}=1$		$\bar{m}=1,\ \bar{n}=2$	
			$a/h=10$	$a/h=20$	$a/h=10$	$a/h=20$
SSSS	UD	M-CST [51]	0.0688	0.0177	0.1638	0.0436
		Present	0.0688	0.0177	0.1637	0.0435
	OD	M-CST [51]	0.0641	0.0164	0.1537	0.0405
		Present	0.0640	0.0164	0.1531	0.0405
	XD	M-CST [51]	0.0730	0.0188	0.1723	0.0463
		Present	0.0732	0.0188	0.1733	0.0464
	VD	M-CST [51]	0.0679	0.0174	0.1618	0.0430
		Present	0.0688	0.0177	0.1637	0.0435
CCCC	UD	M-CST [51]	0.1186	0.0317	0.2286	0.0635
		Present	0.1172	0.0316	0.2228	0.0631
	OD	M-CST [51]	0.1116	0.0295	0.2168	0.0593
		Present	0.1099	0.0294	0.2104	0.0588
	XD	M-CST [51]	0.1243	0.0337	0.2376	0.0673
		Present	0.1237	0.0337	0.2338	0.0670
	VD	M-CST [51]	0.1172	0.0313	0.2262	0.0628
		Present	0.1172	0.0316	0.2228	0.0631

frequencies were achieved by XD and OD dispersion patterns, respectively. Note that, the obtained frequencies by the XD dispersion pattern are about 14% higher than the OD frequencies.

TABLE 8. Non-dimensional frequency $\bar{\omega} = \omega h\sqrt{\rho_m/E_m}$ of the NC plate, $\Lambda_r = 1\%$, $\beta = 0$, $a = b = 10h$, XD.

B.C.	Matrix	Filler	ι/h					
			0.05	0.2	0.4	0.6	0.8	1
SSSS	Pure Epoxy		0.0594	0.0746	0.1087	0.1469	0.1844	0.2194
	Epoxy	G	0.1313	0.1568	0.2176	0.2878	0.3579	0.4238
		GO	0.0703	0.0866	0.1242	0.1667	0.2087	0.2479
		rGO	0.0690	0.0852	0.1224	0.1644	0.2059	0.2446
		Ag/rGO	0.0689	0.0851	0.1223	0.1643	0.2057	0.2444
	Pure CU		0.0594	0.0746	0.1087	0.1469	0.1844	0.2194
	CU	G	0.0824	0.1009	0.1439	0.1926	0.2408	0.2859
		GO	0.0612	0.0766	0.1116	0.1507	0.1891	0.2250
		rGO	0.0605	0.0760	0.1109	0.1500	0.1883	0.2241
		Ag/rGO	0.0604	0.0759	0.1109	0.1499	0.1882	0.2240
CCCC	Pure Epoxy		0.1017	0.1276	0.1831	0.2399	0.2900	0.3316
	Epoxy	G	0.2202	0.2640	0.3620	0.4663	0.5602	0.6393
		GO	0.1195	0.1475	0.2084	0.2717	0.3277	0.3745
		rGO	0.1174	0.1452	0.2055	0.2680	0.3234	0.3695
		Ag/rGO	0.1173	0.1451	0.2053	0.2678	0.3231	0.3692
	Pure CU		0.1017	0.1276	0.1831	0.2399	0.2900	0.3316
	CU	G	0.1398	0.1716	0.2411	0.3136	0.3780	0.4318
		GO	0.1046	0.1311	0.1878	0.2461	0.2974	0.3400
		rGO	0.1035	0.1301	0.1869	0.2451	0.2963	0.3387
		Ag/rGO	0.1034	0.1300	0.1868	0.2449	0.2961	0.3385

Non-dimensional natural frequencies $\bar{\omega} = \omega h\sqrt{\rho_m/E_m}$ of a square plate with $a = b = 10h$ for various material length scale parameters-to-thickness ratios ι/h, boundary conditions, and filler/matrix types are presented in Table 8. XD dispersion pattern and weight fraction $\Lambda_r = 1\%$ are considered. Filler dimensions are $L_r = 2.5\,\mu\text{m}$, $W_r = 1.5\,\mu\text{m}$, $t_r = 1.5\,\text{nm}$ for G, and $L_r = W_r = 1\,\mu\text{m}$, $t_r = 1\,\text{nm}$ for GO, rGO, and Ag/rGO. The presence of filler with excellent mechanical properties embedded in the matrix can lead to a significant increase in stiffness.

As a result, the addition of reinforcements G and GO in the epoxy matrix with $\iota/h = 0.05$ increases the natural frequency $\bar{\omega}$ by 120% and 18%, respectively, while for rGO and Ag/rGO this value is about 16 %. Interestingly, the increase in the material length scale parameter-to-thickness ratio ι/h leads to a decrease in the intensity of this effect, so that the frequency enhancement of the NC plate with $\iota/h = 1$ are 93%, 13%, and 11% for G, GO, and rGO/Ag-rGO, respectively. On the other hand, the reduction of the effect of oxidized and modified

versions of graphene is significantly noticeable compared to graphene. However, the correction of some undesirable issues such as reducing agglomeration, refining filler-matrix bonding, and reducing structural defects are among the benefits of modified and oxidized forms. The presence of filler in the copper matrix with $\iota/h = 0.05$ leads to 39%, 3%, and 1.8% increases in the non-dimensional natural frequency of the NC plate for G, GO, and rGO/Ag-rGO, respectively. These values for $\iota/h = 1$ are reduced to 30%, 2.5%, and 1.5%, respectively. Similar to static bending, it is natural to reduce the filler effect on the metal matrix due to its higher mechanical properties. Along with this character of metals, as mentioned earlier, some issues such as difficulty in achieving proper dispersion of filler in metal matrix and the presence of structural defects have led to less attention to metal matrix composites MMC.

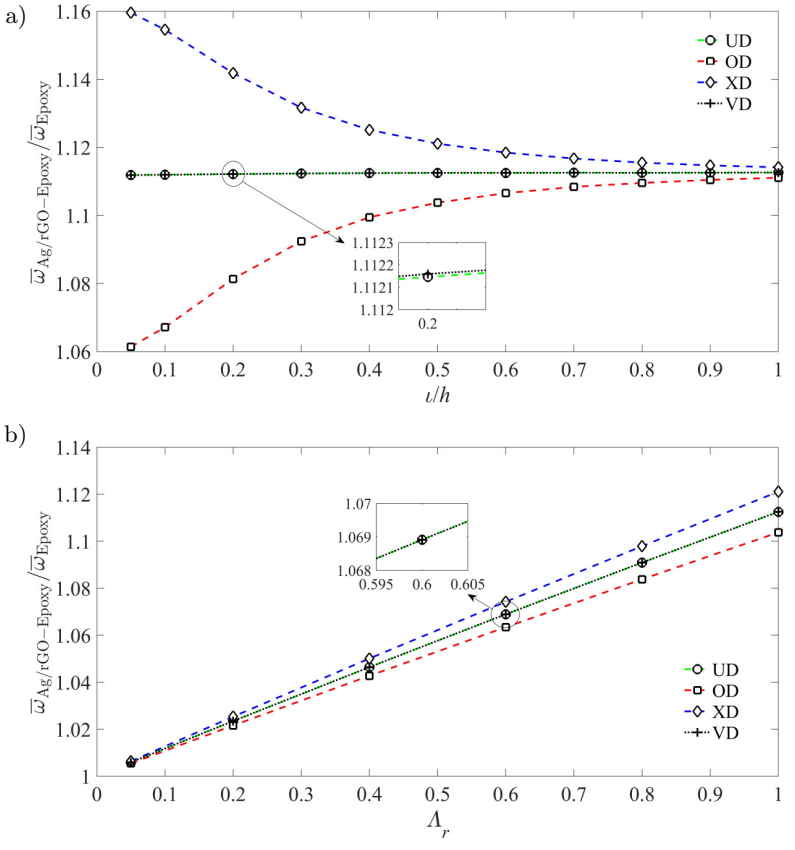

Fig. 5. Effect of various parameters on the non-dimensional natural frequency $\bar{\omega} = \omega h\sqrt{\rho_m/E_m}$ of NC plates: a) natural frequency ratio $\bar{\omega}_{\text{Ag/rGO-Epoxy}}/\bar{\omega}_{\text{Epoxy}}$ versus material length scale parameter to thickness ratio ι/h with $\Lambda_r = 1\%$, b) natural frequency ratio $\bar{\omega}_{\text{Ag/rGO-Epoxy}}/\bar{\omega}_{\text{Epoxy}}$ versus weight fraction $\Lambda_r$with $\iota/h = 0.5$ ($\beta = 0$, $L_r = W_r = 1\,\mu\text{m}$, $t_r = 1\,\text{nm}$, $a = b = 10h$, SSSS).

The results also are depicted in Figs. 5 to 7. Figure 5a shows the non-dimensional natural frequency $\bar{\omega} = \omega h\sqrt{\rho_m/E_m}$ of a simply supported NC plate in the form of $\bar{\omega}_{\text{Ag/rGO-Epoxy}}/\bar{\omega}_{\text{Epoxy}}$ versus material length scale parameter-to-thickness ratio ι/h for various dispersion patterns. Filler dimensions $L_r = W_r = 1\,\mu m$, $t_r = 1\,\text{nm}$ and weight fraction $\Lambda_r = 1\%$ are considered. The length-to-thickness ratio is equal to 10.

As can be seen in Fig. 5a, XD and OD patterns have the largest and smallest effect on NC plate deflection, respectively. However, with the increase of the material length scale parameter to the thickness ratio, the results of the four patterns converge with each other. In this sense, when the small-scale effect becomes obvious, there is no weighty difference between various dispersion patterns concerning natural frequency. Figure 5b illustrates the non-dimensional natural frequency ratio $\bar{\omega}_{\text{Ag/rGO-Epoxy}}/\bar{\omega}_{\text{Epoxy}}$ versus weight fraction Λ_r for various

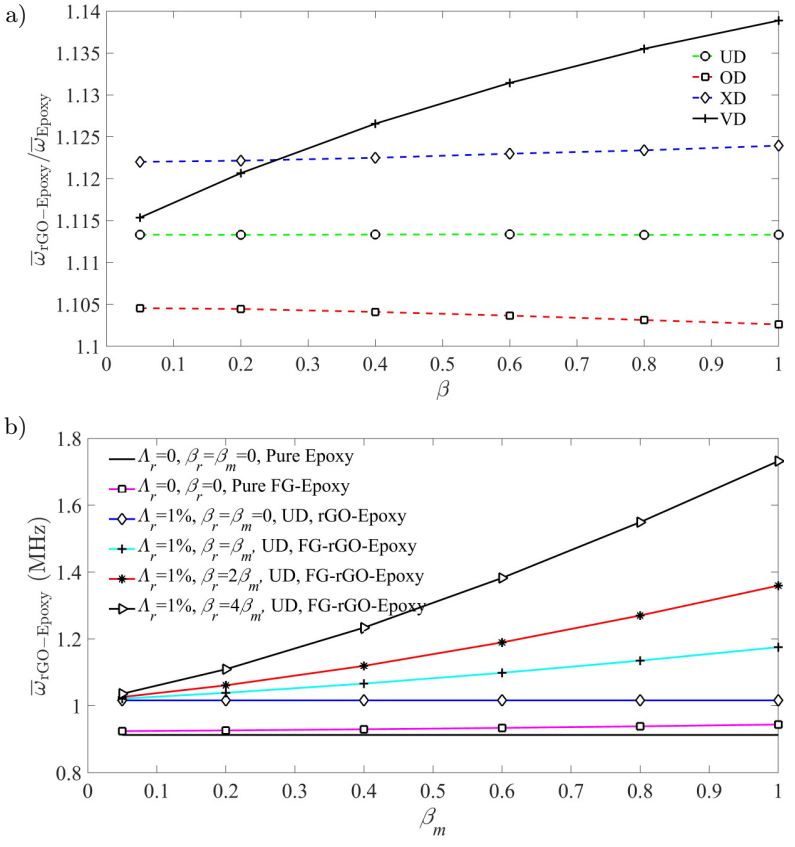

FIG. 6. Effect of various grading index β on the non-dimensional natural frequency ratio $\bar{\omega}_{\text{rGO-Epoxy}}/\bar{\omega}_{\text{Epoxy}}$ of FG-NC plates ($\iota/h = 0.5$, $\bar{\omega} = \omega h\sqrt{\rho_m/E_m}$, $n_r = n_m = 2$, $\Lambda_r = 1\%$, $L_r = W_r = 1\,\mu\text{m}$, $t_r = 1\,\text{nm}$, $a = b = 10h$, SSSS), b) effect of various grading index β_m on the natural frequency $\omega_{\text{rGO-Epoxy}}$ (MHz).

dispersion patterns. As can be seen, increasing the filler weight fraction (up to 1%) leads to impressive growth in the NC plate natural frequency, especially in the XD pattern. Furthermore, OD and VD patterns produce almost identical effects in the homogeneous case ($\beta = 0$).

The effect of grading index β on the natural frequency $\bar{\omega} = \omega h\sqrt{\rho_m/E_m}$ of the simply supported FG-NC plate is presented in Figs. 6a and 6b. The material length scale parameter-to-thickness ratio ι/h and weight fraction Λ_r are 0.5 and 1%, respectively. The length to thickness ratio a/h is equal to 10. Filler dimensions are $L_r = W_r = 1\,\mu\text{m}$, $t_r = 1\,\text{nm}$. The non-dimensional natural frequency ratio $\bar{\omega}_{\text{rGO-Epoxy}}/\bar{\omega}_{\text{Epoxy}}$ of the NC plate for various dispersion patterns is depicted. Interestingly, increasing the grading index leads to an altered rank between the patterns VD and XD as the most effective dispersion scheme in increasing natural frequency.

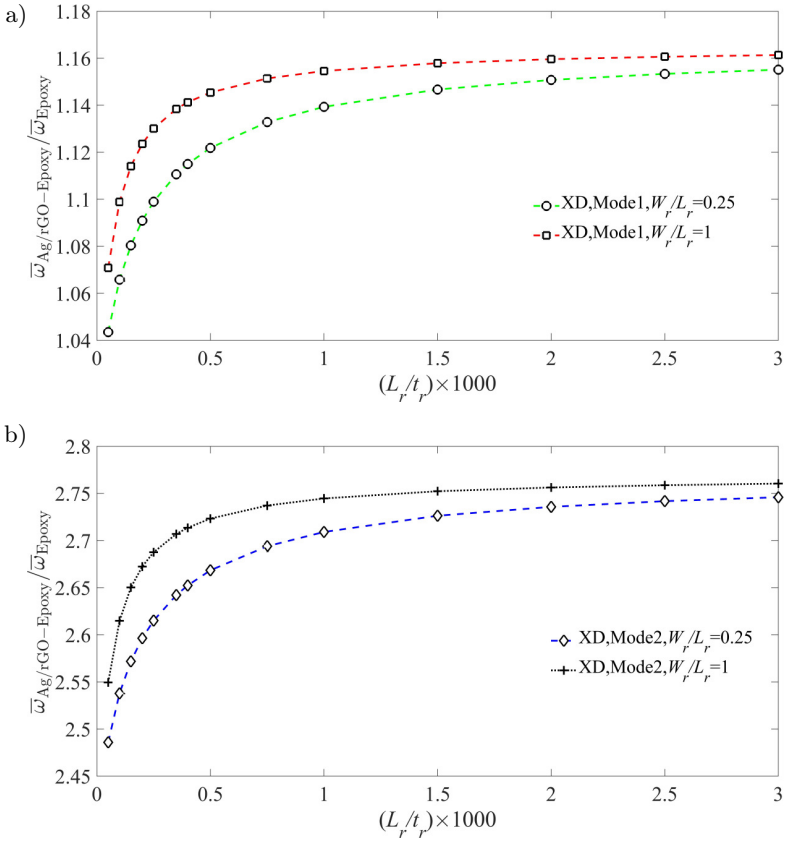

Fig. 7. Effect of various length to thickness ratio of filler L_r/t_r on the natural frequency ratio $\bar{\omega}_{\text{AgrGO-Epoxy}}/\bar{\omega}_{\text{Epoxy}}$ of NC plates: a) first mode, b) second mode ($\iota/h = 0.1$, $\bar{\omega} = \omega h\sqrt{\rho_m/E_m}$, $\Lambda_r = 1\%$, XD, $\beta = 0$, $a = b = 10h$, SSSS).

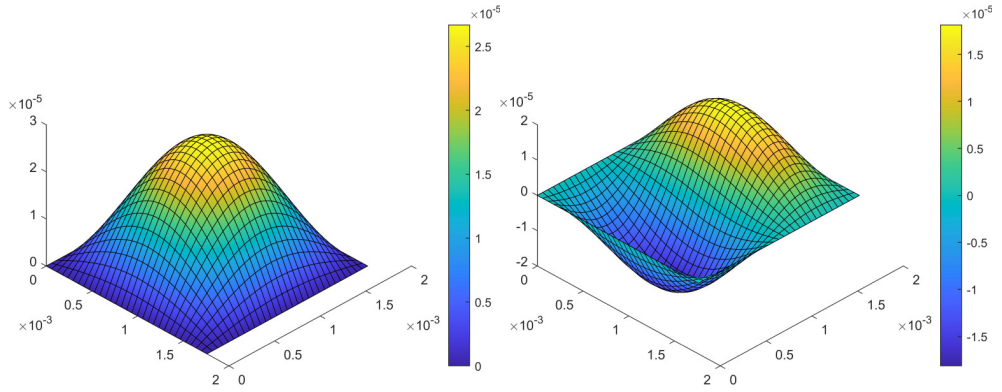

a) $\bar{\omega}_1 = 0.0698$

b) $\bar{\omega}_2 = 0.1664$

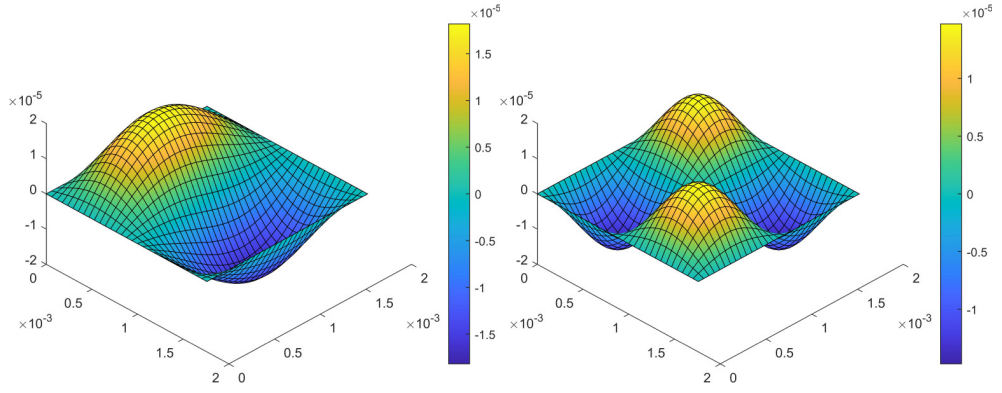

c) $\bar{\omega}_3 = 0.1664$

d) $\bar{\omega}_4 = 0.2552$

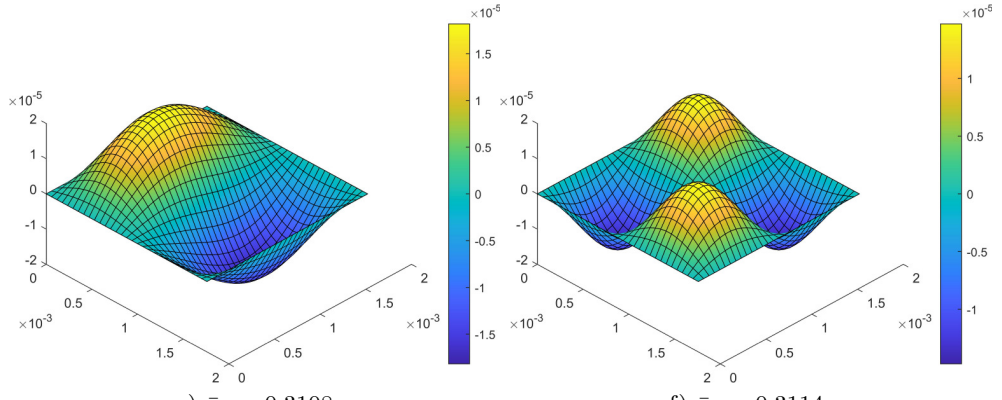

e) $\bar{\omega}_5 = 0.3108$

f) $\bar{\omega}_6 = 0.3114$

FIG. 8. The first six free vibration mode shapes of Ag/rGO-Epoxy NC plates ($\iota/h = 0.1$, $\Lambda_r = 1\%$, UD, $\beta = 0$, $L_r = W_r = 1\,\mu\text{m}$, $t_r = 1\,\text{nm}$, $a = b = 10h$, SSSS).

Figure 7 illustrates the effect of filler dimensions on the NC plate natural frequencies. As demonstrated in the figure, the natural frequency increases by increasing the length-to-thickness ratio of filler L_r/t_r. However, natural fre-

quency enhancement intensity decreases gradually, so that for L_r/t_r greater than 0.001, it almost tends to a constant value. In addition, the increasing effect of the width-to-length ratio of the filler W_r/L_r on the natural frequency also decreases gradually with the increase of the L_r/t_r and the results converge to each other for various W_r/L_r. The first six free vibration mode shapes of Ag/rGO-Epoxy NC plates with UD dispersion patterns are presented in Fig. 8.

6.4. Buckling analysis

The non-dimensional biaxial buckling factors $\bar{\lambda}_{cr} = \lambda_{cr} a^2/E_m h^3$ of rGO/Epoxy NC plate for various length-to-thickness a/h, dispersion patterns, and boundary conditions are presented in Table 9. The rGO properties are considered $E_r = 250\,\text{GPa}$, $\rho_r = 2250\,\text{kg/m}^3$, $\nu_r = 0.165$, $L_r = W_r = 1\,\mu\text{m}$, $t_r = 1\,\text{nm}$ [51]. The material length scale parameter ι is equal to zero. Comparing present results with the other works shows a good agreement between data.

The results show that the non-dimensional buckling factor has a direct relation with the length-to-thickness ratio a/h. Moreover, the largest and lowest values for the buckling factor are captured by XD and OD dispersion patterns, respectively. The XD buckling factor of the NC plate with $a/h = 5$ is about 25% higher than the OD buckling factor which reaches about 32% for $a/h = 100$.

Table 9. Non-dimensional biaxial buckling factor $\bar{\lambda}_{cr} = \lambda_{cr} a^2/E_m h^3$ of rGO/Epoxy NC plate ($N_x^0 = N_y^0 = 1$, $N_{xy}^0 = 0$, $\Lambda_r = 1\%$, $L_r = W_r = 1\,\mu\text{m}$, $t_r = 1\,\text{nm}$, $\beta = 0$, $\iota = 0$, $a = b$).

B.C.	Dispersion pattern	Method	a/h			
			5	10	20	100
SSSS	UD	M-CST [51]	2.0908	2.4432	2.5509	–
		Present	2.0904	2.4441	2.5521	2.5888
	OD	M-CST [51]	1.8689	2.1233	2.1983	–
		Present	1.8463	2.1168	2.1974	2.2245
	XD	M-CST [51]	2.2760	2.7484	2.8993	–
		Present	2.3216	2.7662	2.9053	2.9530
	VD	M-CST [51]	–	–	–	–
		Present	2.0904	2.4440	2.5521	2.5888
CCCC	UD	M-CST [51]	4.2150	5.8283	6.6041	–
		Present	4.1032	5.8448	6.5786	6.8643
	OD	M-CST [51]	3.9259	5.2378	5.7183	–
		Present	3.7309	5.1277	5.6867	5.8994
	XD	M-CST [51]	4.3882	6.5401	7.4628	–
		Present	4.4380	6.5336	7.4597	7.8285
	VD	M-CST [51]	4.1459	5.7925	6.4360	–
		Present	4.1034	5.8448	6.5785	6.8642

TABLE 10. Non-dimensional biaxial buckling factor $\bar{\lambda}_{cr} = \lambda_{cr} a^2/E_m h^3$ of the NC plate ($N_x^0 = N_y^0 = 1$, $N_{xy}^0 = 0$, $\Lambda_r = 1\%$, $\beta = 0$, $a = b = 10h$, XD).

B.C.	Matrix	Filler	ι/h					
			0.05	0.2	0.4	0.6	0.8	1
SSSS	Pure Epoxy		1.8161	2.8553	6.0622	11.0479	17.3655	24.5297
	Epoxy	G	8.8402	12.6082	24.2365	42.3331	65.2974	91.3860
		GO	2.5545	3.8793	7.9673	14.3248	22.3844	31.5291
		rGO	2.4583	3.7468	7.7228	13.9059	21.7440	30.6368
		Ag/rGO	2.4531	3.7396	7.7093	13.8828	21.7086	30.5873
	Pure CU		1.8161	2.8553	6.0622	11.0479	17.3655	24.5297
	CU	G	3.2443	4.8679	9.8777	17.6695	27.5486	38.7598
		GO	1.8952	2.9713	6.2920	11.4546	17.9967	25.4156
		rGO	1.8255	2.8791	6.1299	11.1839	17.5877	24.8492
		Ag/rGO	1.8234	2.8760	6.1239	11.1733	17.5713	24.8263
CCCC	Pure Epoxy		4.3714	6.8458	14.0938	24.3452	35.8652	47.3359
	Epoxy	G	20.6364	29.4026	55.1565	91.8372	133.4110	175.1777
		GO	6.0904	9.2216	18.4024	31.4162	46.0797	60.7208
		rGO	5.8673	8.9152	17.8508	30.5140	44.7780	59.0159
		Ag/rGO	5.8553	8.8985	17.8205	30.4640	44.7058	58.9213
	Pure CU		4.3714	6.8458	14.0938	24.3452	35.8652	47.3359
	CU	G	7.7087	11.5356	22.7600	38.6829	56.6415	74.5915
		GO	4.5587	7.1195	14.6211	25.2328	37.1599	49.0384
		rGO	4.3980	6.9080	14.2597	24.6555	36.3350	47.9617
		Ag/rGO	4.3930	6.9008	14.2460	24.6325	36.3015	47.9176

Table 10 gives the non-dimensional biaxial buckling factor $\bar{\lambda}_{cr} = \lambda_{cr} a^2/E_m h^3$ of a square plate with $a = 10h$ for various material length scale parameter to thickness ratio ι/h, boundary conditions, and filler/matrix type. XD dispersion pattern and weight fraction $\Lambda_r = 1\%$ are considered. Filler dimensions are $L_r = 2.5\,\mu\text{m}$, $W_r = 1.5\,\mu\text{m}$, $t_r = 1.5\,\text{nm}$ for G, and $L_r = W_r = 1\,\mu\text{m}$, $t_r = 1\,\text{nm}$ for GO, rGO, and Ag/rGO.

The obtained results reveal that the addition of dispersed phases G and GO in the epoxy matrix with $\iota/h = 0.05$ increases the buckling factor $\bar{\lambda}_{cr}$ by 380% and 40%, respectively, while for rGO and Ag/rGO, the buckling factor reaches about 35 %. Moreover, the increase in the material length scale parameter-to-thickness ratio ι/h leads to a decrease in the intensity of this effect, so that the buckling factor enhancement of the NC plate with $\iota/h = 1$ is 270%, 28%, and 24% for G, GO, and rGO/Ag-rGO, respectively. Similar to static bending and free vibration, the CU matrix gets a lower level of filler enhancement effect in the buckling case. In this regard, the presence of filler in the copper matrix with $\iota/h = 0.05$ leads to 78%, 4%, and 0.5% increases in the non-dimensional buckling

factor of the NC plate for G, GO, and rGO/Ag-rGO, respectively. These values for $\iota/h = 1$ are reached to 58%, 3.5%, and 0.9%, respectively.

Figures 9 to 11 depict the results. Figure 9a illustrates the non-dimensional biaxial buckling factor $\bar{\lambda}_{cr} = \lambda_{cr} a^2/E_m h^3$ of a simply supported NC plate in the form of $\bar{\lambda}_{\text{Ag/rGO-Epoxy}}/\bar{\lambda}_{\text{Epoxy}}$ versus material length scale parameter-to-thickness ratio ι/h for various dispersion patterns. The length-to-thickness ratio is equal to 10. $L_r = W_r = 1\,\mu\text{m}$, $t_r = 1\,\text{nm}$ and weight fraction $\Lambda_r = 1\%$ are adopted. As can be seen, the greatest and least effects on the NC plate buckling factor are captured by XD and OD patterns, respectively. However, the results of the four patterns meet each other with the increase of the material length scale parameter-to-thickness ratio.

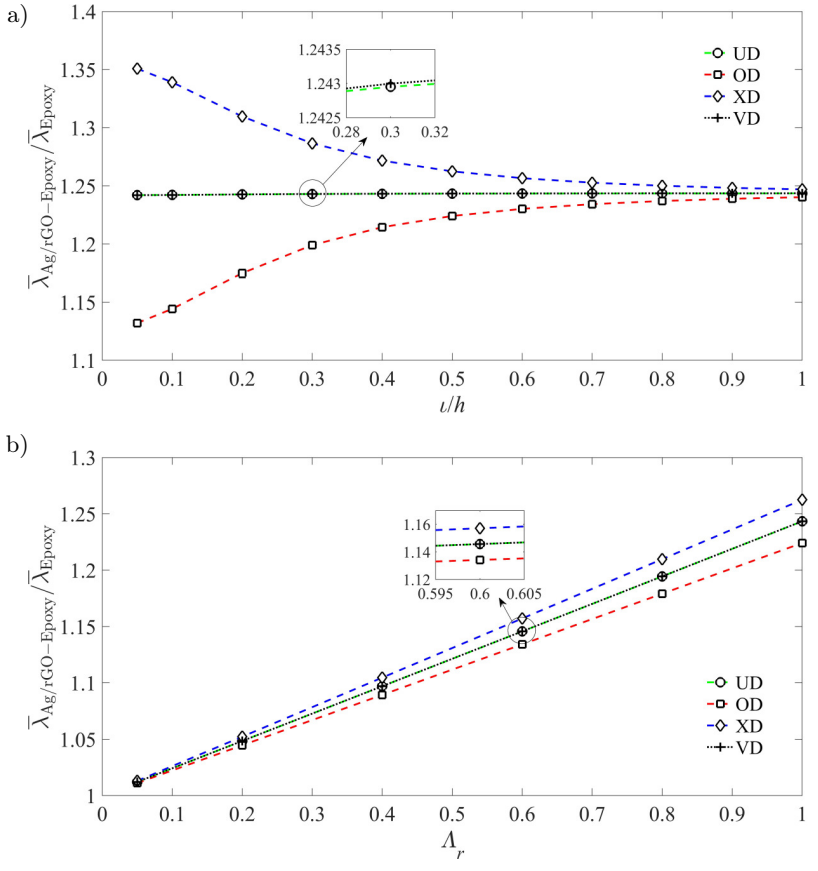

Fig. 9. Effect of various parameters on the non-dimensional biaxial buckling factor $\bar{\lambda}_{cr} = \lambda_{cr} a^2/E_m h^3$ of NC plates: a) buckling factor ratio $\bar{\lambda}_{\text{Ag/rGO-Epoxy}}/\bar{\lambda}_{\text{Epoxy}}$ versus material length scale parameter to thickness ratio ι/h with $\Lambda_r = 1\%$, b) buckling factor ratio $\bar{\lambda}_{\text{Ag/rGO-Epoxy}}/\bar{\lambda}_{\text{Epoxy}}$ versus weight fraction $\Lambda_r$with $\iota/h = 0.5$ ($\beta = 0$, $L_r = W_r = 1\,\mu\text{m}$, $t_r = 1\,\text{nm}$, $a = b = 10h$, SSSS).

This means a noticeable small-scale effect leads to negligible differences between various dispersion patterns concerning buckling factors similar to bending and free vibration cases. Figure 9b provides a good picture of the non-dimensional biaxial buckling factor ratio $\bar{\lambda}_{\text{Ag/rGO-Epoxy}}/\bar{\lambda}_{\text{Epoxy}}$ versus weight fraction Λ_r for various dispersion patterns. As anticipated, increasing the filler weight fraction up to 1% leads to a remarkable increase in the NC plate buckling factor, which is the most severe increase in the XD pattern. Also, OD and VD patterns yield almost the same effects for $\beta = 0$.

The effect of grading index β on the non-dimensional biaxial buckling factor $\bar{\lambda}_{cr} = \lambda_{cr} a^2/E_m h^3$ of a simply supported FG-NC plate is presented in Figs. 10a and 10b. The length-to-thickness ratio a/h is equal to 10. The material length scale parameter-to-thickness ratio ι/h and weight fraction Λ_r are set to be 0.5

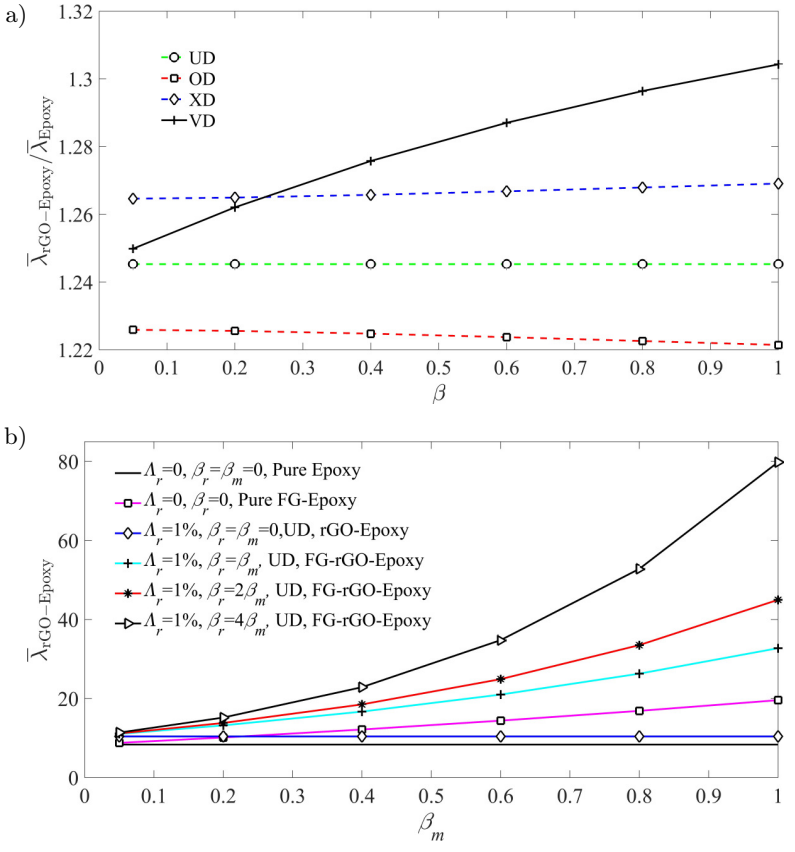

FIG. 10. a) Effect of various grading index β on the buckling factor ratio $\bar{\lambda}_{\text{rGO-Epoxy}}/\bar{\lambda}_{\text{Epoxy}}$ of NC plates ($\bar{\lambda}_{cr} = \lambda_{cr} a^2/E_m h^3$, $\iota/h = 0.5$, $n_r = n_m = 2$, $\Lambda_r = 1\%$, $L_r = W_r = 1\,\mu\text{m}$, $t_r = 1\,\text{nm}$, $a = b = 10h$, SSSS), b) effect of various grading index β_m on the buckling factor $\bar{\lambda}_{\text{rGO-Epoxy}}$.

and 1%, respectively. Filler dimensions are $L_r = W_r = 1\,\mu\text{m}$, $t_r = 1\,\text{nm}$. The non-dimensional buckling factor ratio $\bar{\lambda}_{\text{rGO-Epoxy}}/\bar{\lambda}_{\text{Epoxy}}$ of the NC plate for various dispersion patterns is painted. Remarkably, with the increase of the grading index β, the pattern VD takes the most effective dispersion scheme in increasing the buckling factor.

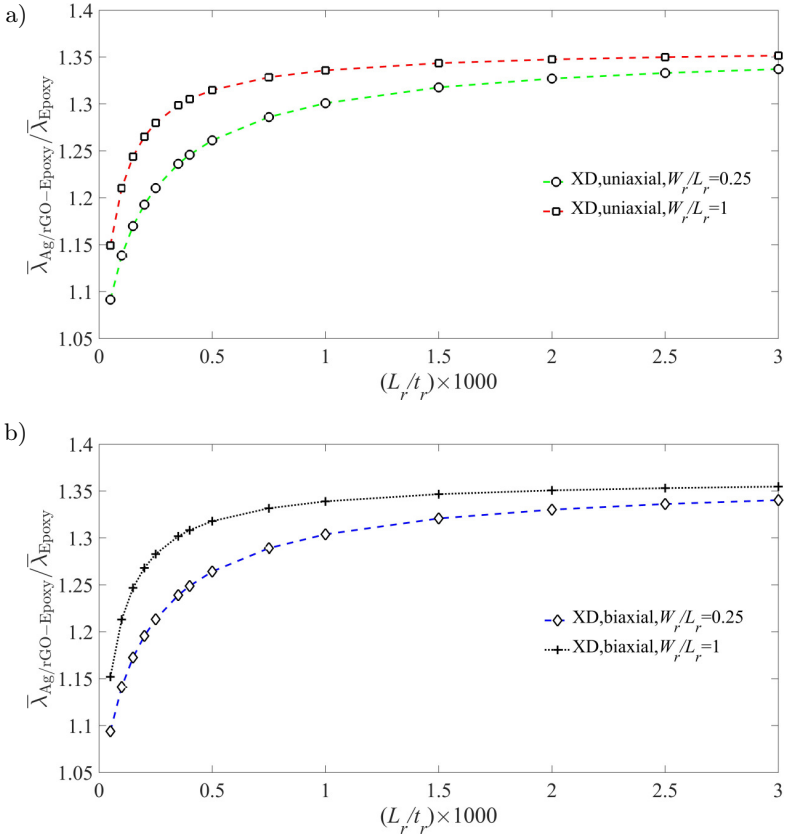

Fig. 11. Effect of various length to thickness ratio of filler L_r/t_r on the buckling factor ratio $\bar{\lambda}_{\text{AgrGO-Epoxy}}/\bar{\lambda}_{\text{Epoxy}}$ of NC plates: a) uniaxial ($N_x^0 = 1$, $N_y^0 = N_{xy}^0 = 0$), b) biaxial ($N_x^0 = N_y^0 = 1$, $N_{xy}^0 = 0$), ($\bar{\lambda}_{cr} = \lambda_{cr} a^2/E_m h^3$, $\beta = 0$, $\iota/h = 0.1$, $\Lambda_r = 1\%$, $a = b = 10h$, SSSS).

Figure 11 illuminates the effect of filler sizes on the NC plate buckling factor. It is clear that the buckling factor increases by increasing the length-to-thickness ratio of the filler L_r/t_r. However, buckling factor enhancement intensity decreases gradually. Moreover, the increasing effect of the width-to-length ratio of filler W_r/L_r on the buckling factor also decreases gradually with the increase of the L_r/t_r, and the results meet each other for various W_r/L_r.

6.5. Optimum parameters

In Table 11, the values of four variables that correspond to the lowest mass of the FG-NC plate model are presented. The lower bound of the first frequency is equal to 0.05 and 10 MH. The graphene-based fillers have a thickness in the nano-range, which can indicate the nano-scale character of the length scale parameter of nanocomposites. However, in most of the works available in the literature, the value of 17.6 μm [66] is used. In this respect, for comparison, two nano values related to the flake, and the platelet have been considered for the characteristic length scale parameter ι, which are equal to 5 nm and 25 nm, respectively.

TABLE 11. The values of four variables correspond to the lowest mass of the FG-NC plate (epoxy, UD, $a = b$, SSSS).

ι	Filler	$\Delta_\iota = \iota/h$	Λ_r	β	$n_a = a/h$	Minimum mass [kg]	ω_1^a [MH]
17.6 μm	GO	0.7651	0.0110	1.0518	6.4757	3.49e-14	0.05
	rGO	0.7652	0.0110	1.0505	6.4682	3.47e-14	0.05
	GO	0.9669	0.0159	1.0394	5.1833	8.72e-15	10
	rGO	0.9704	0.0160	1.0402	5.1621	8.51e-15	10
25 nm	GO	0.7663	0.0110	1.1139	6.8176	1.63e-25	10
	rGO	0.7657	0.0109	1.1085	6.7789	1.61e-25	10
5 nm	GO	0.6637	0.0109	1.1315	6.9148	4.84e-28	10
	rGO	0.6693	0.0109	1.1344	6.9160	4.68e-28	10

7. Conclusion

In this paper, a size-dependent model of functionally graded nanocomposite (FG-NC) Mindlin plates based on the consistent couple stress theory (C-CST) and a non-classical finite element is presented. A unified form is developed for the homogenization of the small-scale heterogeneities of FG-NC plates. In this respect, the Halpin–Tsai model is enriched to capture simultaneously graded behaviour of the elastic properties of the matrix and reinforcement as well as the distribution of the dispersed phases through the plate thickness. A four-node rectangular element is adopted by using the Hermitian approach and in the context of a sub-parametric model to capture the C1 continuity requirements of the couple stress theory. The presented element has 20-DOF at each node, reduced to 12-DOF in a bending mode without stretching deformation. An improved family of graphene including graphene oxide (GO), reduced graphene oxide (rGO), and silver-reduced graphene oxide (Ag-rGO) nano-hybrid are considered. The size-dependent optimization problem is implemented to minimize the FG-NC

plate weight under the frequency constraint, and the corresponding material and geometrical properties of the plate are extracted. The presented model was successfully applied to the bending, free vibration, and buckling analysis of the functionally graded nanocomposite plates, and a set of interesting results are provided that could be a benchmark for future studies.

Appendix A: The strain/curvature-displacement matrix

The strain/curvature-displacement matrix can have the following forms:

(A.1)

$$B_b^0 = [B_{b_1}^0 \ B_{b_2}^0 \ B_{b_3}^0 \ B_{b_4}^0],$$

$$B_{b_i}^0 = \begin{bmatrix} \frac{\partial N_i}{\partial x} & 0 & \frac{\partial N_{ix}}{\partial x} & 0 & \frac{\partial N_{iy}}{\partial x} & 0 & \frac{\partial N_{ixy}}{\partial x} & 0 \\ 0 & \frac{\partial N_i}{\partial y} & 0 & \frac{\partial N_{ix}}{\partial y} & 0 & \frac{\partial N_{iy}}{\partial y} & 0 & \frac{\partial N_{ixy}}{\partial y} \\ \frac{\partial N_i}{\partial y} & \frac{\partial N_i}{\partial x} & \frac{\partial N_{ix}}{\partial y} & \frac{\partial N_{ix}}{\partial x} & \frac{\partial N_{iy}}{\partial y} & \frac{\partial N_{iy}}{\partial x} & \frac{\partial N_{ixy}}{\partial y} & \frac{\partial N_{ixy}}{\partial x} \end{bmatrix},$$

$$B_b^1 = [B_{b_1}^1 \ B_{b_2}^1 \ B_{b_3}^1 \ B_{b_4}^1],$$

$$B_{b_i}^1 = \begin{bmatrix} 0 & \frac{\partial N_i}{\partial x} & 0 & 0 & \frac{\partial N_{ix}}{\partial x} & 0 & 0 & \frac{\partial N_{iy}}{\partial x} & 0 & 0 & \frac{\partial N_{ixy}}{\partial x} & 0 \\ 0 & 0 & \frac{\partial N_i}{\partial y} & 0 & 0 & \frac{\partial N_{ix}}{\partial y} & 0 & 0 & \frac{\partial N_{iy}}{\partial y} & 0 & 0 & \frac{\partial N_{ixy}}{\partial y} \\ 0 & \frac{\partial N_i}{\partial y} & \frac{\partial N_i}{\partial x} & 0 & \frac{\partial N_{ix}}{\partial y} & \frac{\partial N_{ix}}{\partial x} & 0 & \frac{\partial N_{iy}}{\partial y} & \frac{\partial N_{iy}}{\partial x} & 0 & \frac{\partial N_{ixy}}{\partial y} & \frac{\partial N_{ixy}}{\partial x} \end{bmatrix},$$

$$B_s = [B_{s_1} \ B_{s_2} \ B_{s_3} \ B_{s_4}],$$

$$B_{s_i} = \begin{bmatrix} \frac{\partial N_i}{\partial y} & 0 & -N_i & \frac{\partial N_{ix}}{\partial y} & 0 & -N_{ix} & \frac{\partial N_{iy}}{\partial y} & 0 & -N_{iy} & \frac{\partial N_{ixy}}{\partial y} & 0 & -N_{ixy} \\ \frac{\partial N_i}{\partial x} & -N_i & 0 & \frac{\partial N_{ix}}{\partial x} & -N_{ix} & 0 & \frac{\partial N_{iy}}{\partial x} & -N_{iy} & 0 & \frac{\partial N_{ixy}}{\partial x} & -N_{ixy} & 0 \end{bmatrix},$$

(A.2)

$$B_{kb} = -\frac{1}{4} \times [B_{kb_1} \ B_{kb_2} \ B_{kb_3} \ B_{kb_4}],$$

$$B_{kb_i} = \Big[\frac{\partial^2 N_i}{\partial x^2} + \frac{\partial^2 N_i}{\partial y^2} \ \ \frac{\partial N_i}{\partial x} \ \ \frac{\partial N_i}{\partial y} \ \ \frac{\partial^2 N_{ix}}{\partial x^2} + \frac{\partial^2 N_{ix}}{\partial y^2} \ \ \frac{\partial N_{ix}}{\partial x} \ \ \frac{\partial N_{ix}}{\partial y} \ \ \frac{\partial^2 N_{iy}}{\partial x^2} + \frac{\partial^2 N_{iy}}{\partial y^2} \ \ \frac{\partial N_{iy}}{\partial x} \ \ \frac{\partial N_{iy}}{\partial y} \ \ \frac{\partial^2 N_{ixy}}{\partial x^2} + \frac{\partial^2 N_{ixy}}{\partial y^2} \ \ \frac{\partial N_{ixy}}{\partial x} \ \ \frac{\partial N_{ixy}}{\partial y} \Big],$$

$$B_{ks}^0 = -\frac{1}{4} \times [B_{ks_1}^0 \ B_{ks_2}^0 \ B_{ks_3}^0 \ B_{ks_4}^0],$$

$$B_{ks_i}^0 = \begin{bmatrix} \frac{\partial^2 N_i}{\partial y^2} & -\frac{\partial^2 N_i}{\partial x \partial y} & \frac{\partial^2 N_{ix}}{\partial y^2} & -\frac{\partial^2 N_{ix}}{\partial x \partial y} & \frac{\partial^2 N_{iy}}{\partial y^2} & -\frac{\partial^2 N_{iy}}{\partial x \partial y} & \frac{\partial^2 N_{ixy}}{\partial y^2} & -\frac{\partial^2 N_{ixy}}{\partial x \partial y} \\ -\frac{\partial^2 N_i}{\partial x \partial y} & \frac{\partial^2 N_i}{\partial x^2} & -\frac{\partial^2 N_{ix}}{\partial x \partial y} & \frac{\partial^2 N_{ix}}{\partial x^2} & -\frac{\partial^2 N_{iy}}{\partial x \partial y} & \frac{\partial^2 N_{iy}}{\partial x^2} & -\frac{\partial^2 N_{ixy}}{\partial x \partial y} & \frac{\partial^2 N_{ixy}}{\partial x^2} \end{bmatrix},$$

$$B^1_{ks} = \frac{1}{4} \times [B^1_{ks_1}\ B^1_{ks_2}\ B^1_{ks_3}\ B^1_{ks_4}],$$

$$B^1_{ks_i} = \begin{bmatrix} 0 & \frac{\partial^2 N_i}{\partial y^2} & -\frac{\partial^2 N_i}{\partial x \partial y} & 0 & \frac{\partial^2 N_{ix}}{\partial y^2} & -\frac{\partial^2 N_{ix}}{\partial x \partial y} & 0 & \frac{\partial^2 N_{iy}}{\partial y^2} & -\frac{\partial^2 N_{iy}}{\partial x \partial y} \\ 0 & -\frac{\partial^2 N_i}{\partial x \partial y} & \frac{\partial^2 N_i}{\partial x^2} & 0 & -\frac{\partial^2 N_{ix}}{\partial x \partial y} & \frac{\partial^2 N_{ix}}{\partial x^2} & 0 & -\frac{\partial^2 N_{iy}}{\partial x \partial y} & \frac{\partial^2 N_{iy}}{\partial x^2} \\ & & & & & & 0 & \frac{\partial^2 N_{ixy}}{\partial y^2} & -\frac{\partial^2 N_{ixy}}{\partial x \partial y} \\ & & & & & & 0 & -\frac{\partial^2 N_{ixy}}{\partial x \partial y} & \frac{\partial^2 N_{ixy}}{\partial x^2} \end{bmatrix},$$

where $i = 1, 2, 3, 4$.

Appendix B: The pertinent parameters of the global stiffness matrix k, mass matrix M, force vector F, and geometrical stiffness matrix k_g

The pertinent parameters are calculated as follows:

$$\begin{aligned} \hat{k} &= k^1_b + k_s + k_{kb} + k^1_{ks}, \quad \bar{k} = k^0_b + k^0_{ks}, \quad \tilde{k} = k^{01}_b + k^{10}_{ks}, \\ k^1_b &= \int_\Omega {B^1_b}^T D^1_b B^1_b \, d\Omega, \quad k_s = \int_\Omega B^T_s D_s B_s \, d\Omega, \\ k_{kb} &= \int_\Omega B^T_{kb} D_{kb} B_{kb} \, d\Omega, \quad k^1_{ks} = \int_\Omega {B^1_{ks}}^T D^1_{ks} B^1_{ks} \, d\Omega, \\ k^0_b &= \int_\Omega {B^0_b}^T D^0_b B^0_b \, d\Omega, \quad k^0_{ks} = \int_\Omega {B^0_{ks}}^T D^0_{ks} B^0_{ks} \, d\Omega, \\ k^{01}_b &= \int_\Omega {B^1_b}^T D^{01}_b B^0_b \, d\Omega, \quad k^{10}_{ks} = \int_\Omega {B^1_{ks}}^T D^{01}_{ks} B^0_{ks} \, d\Omega, \\ f &= \int_\Omega \hat{N}^T p \, d\Omega + \int_\Gamma \hat{N}^T \bar{t} \, d\Gamma - \int_\Gamma \hat{N}^T \bar{m} \, d\Gamma, \end{aligned} \tag{B.1}$$

$$\hat{M} = \int_\Omega \hat{N}^T M^1 \hat{N} \, d\Omega, \quad \bar{M} = \int_\Omega \bar{N}^T m_0 \bar{N} \, d\Omega, \tag{B.2}$$

$$k^1_g = \int_\Omega B^T_N N \mathrm{B_N} \, d\Omega, \quad B_N = [B_{N_1}\ B_{N_2}\ B_{N_3}\ B_{N_4}],$$

$$B_{N_i} = \begin{bmatrix} \frac{\partial N_i}{\partial x} & 0 & 0 & \frac{\partial N_{ix}}{\partial x} & 0 & 0 & \frac{\partial N_{iy}}{\partial x} & 0 & 0 \\ \frac{\partial N_i}{\partial y} & 0 & 0 & \frac{\partial N_i}{\partial y} & 0 & 0 & \frac{\partial N_i}{\partial y} & 0 & 0 \end{bmatrix}, \tag{B.3}$$

where $p = [p\ 0\ 0]^T$, $\bar{t} = [\bar{t}_z\ 0\ 0]^T$, $\bar{m} = [0\ \bar{m}_x\ \bar{m}_y]^T$.

References

1. B.P. Mishra, D. Mishra, P. Panda, A. Maharana, *An experimental investigation of the effects of reinforcement of graphene fillers on mechanical properties of bi-directional glass/epoxy composite*, Materials Today: Proceedings, **33**, 5429–5441, 2020, doi: 10.1016/J.MATPR.2020.03.154.

2. S. Najafishad, H.D. Manesh, S.M. Zebarjad, N. Hataf, Y. Mazaheri, *Production and investigation of mechanical properties and electrical resistivity of cement-matrix nanocomposites with graphene oxide and carbon nanotube reinforcements*, Archives of Civil and Mechanical Engineering, **20**, 2, 57, 2020, doi: 10.1007/S43452-020-00059-5/METRICS.

3. Z. Hu, G. Tong, D. Lin, C. Chen, H. Guo, J. Xu, L. Zhou, *Graphene-reinforced metal matrix nanocomposites – a review*, Materials Science and Technology, **32**, 9, 930–953, 2016, doi: 10.1080/02670836.2015.1104018.

4. G. Mittal, V. Dhand, K.Y. Rhee, S.J. Park, W.R. Lee, *A review on carbon nanotubes and graphene as fillers in reinforced polymer nanocomposites*, Journal of Industrial and Engineering Chemistry, **21**, 11–25, 2015, doi: 10.1016/J.JIEC.2014.03.022.

5. G.A. Maugin, A.V. Metrikine, *Mechanics of generalized continua: one hundred years after the Cosserats*, Springer Science & Business Media, New York, 2010, doi: 10.1007/978-1-4419-5695-8.

6. A.C. Eringen, *Nonlocal continuum field theories*, Springer Science & Business Media, New York, 2002, doi: 10.1007/b97697.

7. A.C. Eringen, *Microcontinuum Field Theories*, Springer Science & Business Media, New York, 1999, doi: 10.1007/978-1-4612-0555-5.

8. R.D. Mindlin, H.F. Tiersten, *Effects of couple-stresses in linear elasticity*, Archive for Rational Mechanics and Analysis, **11**, 1, 415–448, 1962, doi: 10.1007/BF00253946.

9. R.D. Mindlin, *Influence of couple-stresses on stress concentrations*, Experimental Mechanics, **3**, 1, 1–7, 1963, doi: 10.1007/bf02327219.

10. F. Yang, A.C.M. Chong, D.C.C. Lam, P. Tong, *Couple stress based strain gradient theory for elasticity*, International Journal of Solids and Structures, **39**, 10, 2731–2743, 2002, doi: 10.1016/S0020-7683(02)00152-X.

11. H. Wang, Z. Li, S. Zheng, *Size-dependent deflection of cross-ply composite laminated plate induced by piezoelectric actuators based on a re-modified couple stress theory*, Archives of Mechanics, **71**, 3, 177–205, 2019, doi: 10.24423/AOM.3047.

12. I. Eshraghi, S. Dag, *Transient dynamic analysis of functionally graded micro-beams considering small-scale effects*, Archives of Mechanics, **73**, 4, 303–337, 2021, doi: 10.24423/AOM.3786.

13. A.R. Hadjesfandiari, G.F. Dargush, *Couple stress theory for solids*, International Journal of Solids and Structures, **48**, 18, 2496–2510, 2011, doi: 10.1016/J.IJSOLSTR.2011.05.002

14. A.R. Hadjesfandiari, G.F. Dargush, *Fundamental solutions for isotropic size-dependent couple stress elasticity*, International Journal of Solids and Structures, **50**, 9, 1253–1265, 2013, doi: 10.1016/J.IJSOLSTR.2012.12.021.

15. A.R. HADJESFANDIARI, *Character of couple and couple-stress in continuum mechanics*, 2022, doi: 10.48550/arXiv.2202.02152.

16. A. HAJESFANDIARI, A.R. HADJESFANDIARI, G.F. DARGUSH, *Boundary element formulation for plane problems in size-dependent piezoelectricity*, International Journal for Numerical Methods in Engineering, **108**, 7, 667–694, 2016, doi: 10.1002/nme.5227.

17. B.T. DARRALL, A.R. HADJESFANDIARI, G.F. DARGUSH, *Size-dependent piezoelectricity*: *A 2D finite element formulation for electric field-mean curvature coupling in dielectrics*, European Journal of Mechanics - A/Solids, **49**, 308–320, 2015, doi: 10.1016/j.euromechsol.2014.07.013.

18. A.R. HADJESFANDIARI, *Size-dependent piezoelectricity*, International Journal of Solids and Structures, **50**, 18, 2781–2791, 2013, doi: 10.1016/J.IJSOLSTR.2013.04.020.

19. A.R. HADJESFANDIARI, *Size-dependent thermoelasticity*, Latin American Journal of Solids and Structures, **11**, 9, 1679–1708, 2014, doi: 10.1590/S1679-78252014000900010.

20. H. VAGHEFPOUR, H. ARVIN, *Nonlinear free vibration analysis of pre-actuated isotropic piezoelectric cantilever Nano-beams*, Microsystem Technologies, **25**, 11, 4097–4110, 2019, doi: 10.1007/S00542-019-04351-0/METRICS.

21. G. DENG, G.F. DARGUSH, *Mixed variational principle and finite element formulation for couple stress elastostatics*, International Journal of Mechanical Sciences, **202**, 106497, 2021, doi: 10.1016/j.ijmecsci.2021.106497.

22. F. ABBASPOUR, H. ARVIN, *Vibration and thermal buckling analyses of three-layered centrosymmetric piezoelectric microplates based on the modified consistent couple stress theory*, Journal of Vibration and Control, **26**, 15–16, 1253–1265, 2020, doi: 10.1177/1077546320924273.

23. B.N. PATEL, D. PANDIT, S.M. SRINIVASAN, *A simplified moment-curvature based approach for large deflection analysis of micro-beams using the consistent couple stress theory,* European Journal of Mechanics – A/Solids, **66**, 45–54, 2017, doi: 10.1016/J.EUROMECHSOL.2017.06.002.

24. A.R. HADJESFANDIARI, G.F. DARGUSH, *Comparison of theoretical elastic couple stress predictions with physical experiments for pure torsion*, 2016, doi: 10.48550/arXiv.1605.02556.

25. R. SOROUSH, A. KOOCHI, M. KEIVANI, M. ABADYAN, *A bilayer model for incorporating the coupled effects of surface energy and microstructure on the electromechanical stability of NEMS*, International Journal of Structural Stability and Dynamics, **17**, 1771005, 2017, doi: 10.1142/S0219455417710055.

26. A.K. GEIM, K.S. NOVOSELOV, *The rise of graphene*, Nature Materials, **6**, 3, 183–191, 2007, doi: 10.1038/nmat1849.

27. P. AVOURIS, C. DIMITRAKOPOULOS, *Graphene: synthesis and applications*, Materials Today, **15**, 3, 86–97, 2012, doi: 10.1016/S1369-7021(12)70044-5.

28. A.M. DIMIEV, S. EIGLER, *Graphene Oxide: Fundamentals and Applications*, John Wiley & Sons, 2016, doi: 10.1002/9781119069447.

29. Y. GUO, X. YANG, K. RUAN, J. KONG, M. DONG, J. ZHANG, J. GU, Z. GUO, *Reduced graphene oxide heterostructured silver nanoparticles significantly enhanced thermal conductivities in hot-pressed electrospun polyimide nanocomposites*, ACS Applied Materials & Interfaces, **11**, 28, 25465–25473, 2019, doi: 10.1021/acsami.9b10161.

30. S.K. Krishnan, E. Singh, P. Singh, M. Meyyappan, H.S. Nalwa, *A review on graphene-based nanocomposites for electrochemical and fluorescent biosensors*, RSC Advances, **9**, 16, 8778–8881, 2019, doi: 10.1039/C8RA09577A.

31. T. Yang, W. Chen, F. Yan, H. Lu, Y.Q. Fu, *Effect of reduced graphene oxides decorated by Ag and Ce on mechanical properties and electrical conductivity of copper matrix composites*, Vacuum, **183**, 109861, 2021, doi: 10.1016/J.VACUUM.2020.109861.

32. A. Kumar Srivastava, D. Kumar, *Postbuckling behaviour of graphene-reinforced plate with interfacial effect*, Archives of Mechanics, **70**, 1, 3–36, 2018, doi: 10.24423/AOM.2796.

33. T. Farsadi, D. Asadi, H. Kurtaran, *Frequency study of functionally graded multilayer graphene platelet-reinforced polymer cylindrical panels*, Archives of Mechanics, **73**, 5–6, 471–498, 2021, doi: 10.24423/AOM.3761.

34. Q. Qian, Y. Wang, F. Zhu, C. Feng, J. Yang, S. Wang, *Primary nonlinear damped natural frequency of dielectric composite beam reinforced with graphene platelets (GPLs)*, Archives of Civil and Mechanical Engineering, **22**, 1, 53, 2022, doi: 10.1007/S43452-021-00369-2/METRICS.

35. N. Guarín-Zapata, J. Gomez, A.R. Hadjesfandiari, G.F. Dargush, *Variational principles and finite element Bloch analysis in couple stress elastodynamics*, Wave Motion, **106**, 102809, 2021, doi: 10.1016/J.WAVEMOTI.2021.102809.

36. G.F. Dargush, G. Apostolakis, A.R. Hadjesfandiari, *Two- and three-dimensional size-dependent couple stress response using a displacement-based variational method*, European Journal of Mechanics - A/Solids, **88**, 104268, 2021, doi: 10.1016/J.EUROMECHSOL.2021.104268.

37. G. Apostolakis, G.F. Dargush, *Size-dependent couple stress natural frequency analysis via a displacement-based variational method for two- and three-dimensional problems*, Acta Mechanica, **234**, 3, 891–910, 2023, doi: 10.1007/S00707-022-03421-1/METRICS.

38. H.X. Nguyen, T.N. Nguyen, M. Abdel-Wahab, S.P.A. Bordas, H. Nguyen-Xuan, T.P. Vo, *A refined quasi-3D isogeometric analysis for functionally graded microplates based on the modified couple stress theory*, Computer Methods in Applied Mechanics and Engineering, **313**, 904–940, 2017, doi: 10.1016/J.CMA.2016.10.002.

39. A. Farzam, B. Hassani, *Isogeometric analysis of in-plane functionally graded porous microplates using modified couple stress theory*, Aerospace Science and Technology, **91**, 508–524, 2019, doi: 10.1016/J.AST.2019.05.012.

40. H.M. Ma, X.L. Gao, J.N. Reddy, *A non-classical Mindlin plate model based on a modified couple stress theory*, Acta Mechanica, **220**, 1–4, 217–235, 2011, doi: 10.1007/S00707-011-0480-4/METRICS.

41. B. Zhang, Y. He, D. Liu, Z. Gan, L. Shen, *A non-classical Mindlin plate finite element based on a modified couple stress theory*, European Journal of Mechanics - A/Solids, **42**, 63–80, 2013, doi: 10.1016/J.EUROMECHSOL.2013.04.005.

42. C.H. Thai, A.J.M. Ferreira, T.D. Tran, P. Phung-Van, *A size-dependent quasi-3D isogeometric model for functionally graded graphene platelet-reinforced composite microplates based on the modified couple stress theory*, Composite Structures, **234**, 111695, 2020, doi: 10.1016/J.COMPSTRUCT.2019.111695.

43. C.P. Wu, H.X. Hu, *A unified size-dependent plate theory for static bending and free vibration analyses of micro- and nano-scale plates based on the consistent couple stress theory*, Mechanics of Materials, **162**, 104085, 2021, doi: 10.1016/J.MECHMAT.2021.104085.

44. C.P. Wu, E.-L. Lin, *Free vibration analysis of porous functionally graded piezoelectric microplates resting on an elastic medium subjected to electric voltages*, Archives of Mechanics, **74**, 6, 463–511, 2022, doi: 10.24423/AOM.4150.

45. C.P. Wu, Y.A. Lu, *A hermite-family c1 finite layer method for the three-dimensional free vibration analysis of exponentially graded piezoelectric microplates based on the consistent couple stress theory*, International Journal of Structural Stability and Dynamics, **23**, 4, 2350044, 2023, doi: 10.1142/S021945542350044X.

46. C.P. Wu, Y.S. Lyu, *An asymptotic consistent couple stress theory for the three-dimensional free vibration analysis of functionally graded microplates resting on an elastic medium*, Mathematical Methods in the Applied Sciences, **46**, 4, 4891–4919, 2023, doi: 10.1002/MMA.8810.

47. C.P. Wu, C.H. Hsu, *A three-dimensional weak formulation for stress, deformation, and free vibration analyses of functionally graded microscale plates based on the consistent couple stress theory*, Composite Structures, **296**, 115829, 2022, doi: 10.1016/J.COMPSTRUCT.2022.115829.

48. C.P. Wu, Y.A. Lu, *3D static bending analysis of functionally graded piezoelectric microplates resting on an elastic medium subjected to electro-mechanical loads using a size-dependent Hermitian C 2 finite layer method based on the consistent couple stress theory*, Mechanics Based Design of Structures and Machines, 1–43, 2023, doi: 10.1080/15397734.2023.2209633.

49. H.P. Wu, Y. Shang, S. Cen, C.F. Li, *Penalty C0 8-node quadrilateral and 20-node hexahedral elements for consistent couple stress elasticity based on the unsymmetric finite element method*, Engineering Analysis with Boundary Elements, **147**, 302–319, 2023, doi: 10.1016/J.ENGANABOUND.2022.12.008.

50. Y.H. Mao, Y. Shang, Y.D. Wang, *Non-conforming Trefftz finite element implementation of orthotropic Kirchhoff plate model based on consistent couple stress theory*, Acta Mechanica, **234**, 5, 1857–1887, 2023, doi: 10.1007/S00707-023-03479-5/TABLES/13.

51. A. Farzam, B. Hassani, *Isogeometric analysis of FG polymer nanocomposite plates reinforced with reduced graphene oxide using MCST*, Advances in Aircraft and Spacecraft Science, **9**, 1, 69–93, 2022, doi: 10.12989/aas.2022.9.1.069.

52. M.A. Roudbari, T.D. Jorshari, C. Lu, R. Ansari, A.Z. Kouzani, M. Amabili, *A review of size-dependent continuum mechanics models for micro- and nano-structures,* Thin-Walled Structures, **170**, 108562, 2022, doi: 10.1016/J.TWS.2021.108562.

53. J. Reddy, *Theory and analysis of elastic plates and shells*, CRC press, 2006, doi: 10.1201/9780849384165.

54. M. Asghari, *Geometrically nonlinear micro-plate formulation based on the modified couple stress theory*, International Journal of Engineering Science, **51**, 292–309, 2012, doi: 10.1016/J.IJENGSCI.2011.08.013.

55. J.N. Reddy, J. Berry, *Nonlinear theories of axisymmetric bending of functionally graded circular plates with modified couple stress*, Composite Structures, **94**, 12, 3664–3668, 2012, doi: 10.1016/J.COMPSTRUCT.2012.04.019.

56. K.F. Wang, T. Kitamura, B. Wang, *Nonlinear pull-in instability and free vibration of micro/nanoscale plates with surface energy – A modified couple stress theory model*, International Journal of Mechanical Sciences, **99**, 288–296, 2015, doi: 10.1016/J.IJMECSCI.2015.05.006.

57. M.Z. Roshanbakhsh, S.M. Tavakkoli, B. Navayi Neya, *Free vibration of functionally graded thick circular plates: An exact and three-dimensional solution*, International Journal of Mechanical Sciences, **188**, 105967, 2020, doi: 10.1016/J.IJMECSCI.2020.105967.

58. S. Zhao, Z. Zhao, Z. Yang, L.L. Ke, S. Kitipornchai, J. Yang, *Functionally graded graphene reinforced composite structures: A review*, Engineering Structures, **210**, 110339, 2020, doi: 10.1016/J.ENGSTRUCT.2020.110339.

59. M.A. Rafiee, J. Rafiee, Z. Wang, H. Song, Z.Z. Yu, N. Koratkar, *Enhanced mechanical properties of nanocomposites at low graphene content*, ACS Nano, **3**, 12, 3884–3890, 2009, doi: 10.1021/NN9010472.

60. J.C. Haplin, J.L. Kardos, *The Halpin–Tsai equations: A review*, Polymer Engineering & Science, **16**, 5, 344–352, 1976, doi: 10.1002/pen.760160512.

61. J.C. Halpin, R.L. Thomas, *Ribbon reinforcement of composites*, Journal of Composite Materials, **2**, 4, 488–497, 1968, doi: 10.1177/002199836800200409.

62. F. Ebrahimi, A. Dabbagh, *Mechanics of nanocomposites?: homogenization and analysis*, CRC Press, 2020, doi: 10.1201/9780429316791.

63. J.N. Reddy, *Introduction to the Finite Element Method*, McGraw-Hill Education, 2005.

64. F.K. Bogner, R.L. Fox, L.A. Schmit, *The generation of interelement compatible stiffness and mass matrices by the use of interpolation formulae*, Proceedings of the First Conference on Matrix Methods in Structural Mechanics AFFDL-TR-66-80, 1966.

65. A. Adini, R.W. Clough, *Analysis of plate Bending by the Finite Element Method*, University of California, California, 1960.

66. D.C.C. Lam, F. Yang, A.C.M. Chong, J. Wang, P. Tong, *Experiments and theory in strain gradient elasticity*, Journal of the Mechanics and Physics of Solids, **51**, 8, 1477–1508, 2003, doi: 10.1016/S0022-5096(03)00053-X.

67. X. Liu, Q. Yang, *Molecular dynamic simulation of mechanical behaviour of RGO produced by thermal reduction method*, Micro & Nano Letters, **12**, 9, 638–642, 2017, doi: 10.1049/MNL.2017.0072.

68. J. Wan, J.W. Jiang, H.S. Park, *Negative Poisson's ratio in graphene oxide*, Nanoscale, **9**, 11, 4007–4012, 2017, doi: 10.1039/C6NR08657H.

69. M.R. Safaei, H.R. Goshayeshi, I. Chaer, *Solar still efficiency enhancement by using graphene oxide/paraffin nano-PCM*, Energies (Basel), **12**, 10, 2002, 2019, doi: 10.3390/EN12102002.

70. M.F. Ashby, D.R.H. Jones, *Engineering Materials 1: An Introduction to Properties, Applications, and Design*, Elsevier, 2012, doi: 10.1016/C2009-0-64288-4.

71. G.C. Tsiatas, *A new Kirchhoff plate model based on a modified couple stress theory*, International Journal of Solids and Structures, **46**, 13, 2757–2764, 2009, doi: 10.1016/J.IJSOLSTR.2009.03.004.

72. H.T. Thai, S.E. Kim, *A size-dependent functionally graded Reddy plate model based on a modified couple stress theory,* Composites Part B: Engineering, **45**, 1, 1636–1645, 2013, doi: 10.1016/J.COMPOSITESB.2012.09.065.

73. H. Salehipour, H. Nahvi, A.R. Shahidi, H.R. Mirdamadi, *3D elasticity analytical solution for bending of FG micro/nanoplates resting on elastic foundation using*

modified couple stress theory, Applied Mathematical Modelling, **47**, 174–188, 2017, doi: 10.1016/J.APM.2017.03.007.

74. H.T. THAI, D.H. CHOI, *Size-dependent functionally graded Kirchhoff and Mindlin plate models based on a modified couple stress theory*, Composite Structures, **95**, 142–153, 2013, doi: 10.1016/J.COMPSTRUCT.2012.08.023.

Received December 7, 2023; revised version March 25, 2024.
Published online April 23, 2024.